Multiply lensed star forming clumps in the A521-sys1 galaxy at redshift 1

Matteo Messa, Miroslava Dessauges-Zavadsky, Johan Richard, Angela Adamo, David Nagy, Françoise Combes, Lucio Mayer, Harald Ebeling

Monthly Notices of the ROYAL ASTRONOMICAL SOCIETY

MNRAS **516,** 2420–2443 (2022) https://doi.org/10.1093/mnras/stac2189
Advance Access publication 2022 August 4

Multiply lensed star forming clumps in the A521-sys1 galaxy at redshift 1

Matteo Messa [1,2]★ Miroslava Dessauges-Zavadsky [1] Johan Richard [3] Angela Adamo,[2] David Nagy,[1] Françoise Combes,[4] Lucio Mayer[5] and Harald Ebeling [6]

[1]*Observatoire de Genève, Université de Genève, Versoix, Switzerland*
[2]*The Oskar Klein Centre, Department of Astronomy, Stockholm University, AlbaNova, SE-10691 Stockholm, Sweden*
[3]*Univ Lyon, Univ Lyon1, ENS de Lyon, CNRS, Centre de Recherche Astrophysique de Lyon UMR5574, Saint-Genis-Laval, France*
[4]*LERMA, Observatoire de Paris, PSL Research Université, CNRS, Sorbonne Université, UPMC, Paris, France*
[5]*Center for Theoretical Astrophysics and Cosmology, Institute for Computational Science, University of Zurich, Winterthurerstrasse 190, CH-8057 Zürich, Switzerland*
[6]*Institute for Astronomy University of Hawaii, 2680 Woodlawn Drive Honolulu, HI 96822, USA*

Accepted 2022 July 29. Received 2022 July 26; in original form 2022 March 29

ABSTRACT

We study the population of star-forming clumps in A521-sys1, a $z = 1.04$ system gravitationally lensed by the foreground ($z = 0.25$) cluster Abell 0521. The galaxy presents one complete counter-image with a mean magnification of $\mu \sim 4$ and a wide arc containing two partial images of A521-sys1 with magnifications reaching $\mu > 20$, allowing the investigations of clumps down to scales of $R_{eff} < 50$ pc. We identify 18 unique clumps with a total of 45 multiple images. Intrinsic sizes and UV magnitudes reveal clumps with elevated surface brightnesses comparable to similar systems at redshifts $z \gtrsim 1.0$. Such clumps account for ∼40 per cent of the galaxy UV luminosity implying a significant fraction of the recent star-formation activity is taking place there. Clump masses range from 10^6 to 10^9 $M_\odot$ and sizes from tens to hundreds of parsec resulting in mass surface densities from 10 to 10^3 $M_\odot$ pc^{-2} with a median of $\sim 10^2$ $M_\odot$ pc^{-2}. These properties suggest that we detect star formation taking place across a wide range of scale from cluster aggregates to giant star-forming complexes. We find ages of less than 100 Myr consistent with clumps being observed close to their natal region. The lack of galactocentric trends with mass, mass density, or age and the lack of old migrated clumps can be explained either by dissolution of clumps after few ∼100 Myr or by stellar evolution making them fall below the detectability limits of our data.

Key words: gravitational lensing: strong – galaxies: high-redshift – galaxies: individual: A521-sys1 – galaxies: star clusters – galaxies: star formation.

1 INTRODUCTION

The study of galaxies at Cosmic Noon (redshift $z \sim 1$–3) reveals morphologies dominated by clumpy structures, particularly at rest-frame ultraviolet (UV) wavelengths (e.g. Cowie, Hu & Songaila 1995; van den Bergh et al. 1996). Clumps have typical sizes of $\lesssim$1 kpc (e.g. Elmegreen et al. 2007; Förster Schreiber et al. 2011b), typical stellar masses of $M_* \sim 10^7$–10^9 $M_\odot$ (e.g. Förster Schreiber et al. 2011a; Guo et al. 2012; Soto et al. 2017) and typical star-formation rates (SFRs) from 0.1–10 $M_\odot$ yr^{-1} (e.g. Guo et al. 2012; Soto et al. 2017). The presence of UV clumps is closely related to gas properties observed in those galaxies characterized by higher gas fractions (Daddi et al. 2010; Tacconi et al. 2010, 2013; Genzel et al. 2015) and velocity dispersions (Elmegreen & Elmegreen 2005; Förster Schreiber et al. 2006) than local main sequence (MS) star-forming galaxies, yet, overall they show rotation features indicating the presence of disc structure (Förster Schreiber et al. 2006; Genzel et al. 2006; Shapiro et al. 2008; Wisnioski et al. 2018). The commonly accepted interpretation of these findings is that clumps result from *in situ* gas collapse due to gravitational instabilities in the disc, which can fragment at much larger scales at high redshift than in local MS galaxies because of the gas-rich turbulent composition of these objects (e.g Immeli et al. 2004b; Elmegreen et al. 2009; Tamburello et al. 2015; Renaud, Romeo & Agertz 2021). This interpretation is supported by recent observations of dense giant molecular cloud complexes from CO data in galaxies at $z \sim 1$ (Dessauges-Zavadsky et al. 2019), as well as by simulations of turbulent high-redshift galaxies (e.g. van Donkelaar, Agertz & Renaud 2021) and by observations in nearby analogs (e.g. Fisher et al. 2017a, b; Messa et al. 2019).

An additional confirmation of the link between clumps and their host galaxies is given by the evolution of the clump densities with redshift (clumps are denser at higher redshifts), tracing the evolution of star formation (SF) with cosmological time (Livermore et al. 2015). We note though that the interpretation of the underlying observations is complicated by the difference in surface-brightness completeness limits (Ma et al. 2018), and the different resolution achievable at different redshifts and at different gravitational lensing magnifications.

In addition, high-redshift clumps may affect the process of galaxy assembly, hydro-dynamical, and cosmological simulations have suggested that, if clumps are able to survive as bound systems for

★ E-mail: matteo.messa@unige.ch

hundreds of Myr, dynamical friction could cause them to migrate toward the centre of the galaxy (Bournaud et al. 2014; Mandelker et al. 2014, 2017). Such spiralling inward would generate torque that, in turn, funnels inward large amounts of gas, which, along with clump merging could contribute to the formation of the thick galactic disc and to the bulge growth (Noguchi 1999; Immeli et al. 2004a; Bournaud, Elmegreen & Elmegreen 2007; Carollo et al. 2007; Elmegreen, Bournaud & Elmegreen 2008; Genzel et al. 2008; Bournaud, Elmegreen & Martig 2009; Dekel, Sari & Ceverino 2009; Bournaud et al. 2011; Gabor & Bournaud 2013). However, not all simulations predict clumps surviving for long time-scales (Oklopčić et al. 2017). Observations of individual galaxies seem to support this scenario (e.g. Guo et al. 2012; Adamo et al. 2013; Cava et al. 2018), but the large uncertainties on age determinations and the lack of larger statistical samples prevent us from assessing if, and in what conditions, clumps could survive long enough to migrate from their natal region.

High-redshift clumps contribute by a large fraction to the emission in the rest-frame UV (Elmegreen et al. 2005) and in nebular lines (e.g. Balmer transitions, Livermore et al. 2012; Mieda et al. 2016; Zanella et al. 2019) of their host galaxies, suggesting that they trace giant star-forming regions and that those regions constitute the bulk of their host galaxy's recent star-formation activity. Due to their elevated specific star-formation rate (sSFR = SFR/M_*), which can exceed the integrated sSFR of their host galaxies by orders of magnitude, it has been suggested that clumps are starbursting (Bournaud et al. 2015; Zanella et al. 2015, 2019). We expect feedback from star-forming clumps to affect the evolution of galaxies suppressing the global star formation and leading to the formation of a multiphase interstellar medium (ISM) (e.g Hopkins, Quataert & Murray 2012; Goldbaum, Krumholz & Forbes 2016). Evidence from local analogs suggests that stellar feedback from clumps could facilitate the escape of UV radiation into the intergalactic medium (e.g. Bik et al. 2015, 2018; Herenz et al. 2017 in local galaxies, Rivera-Thorsen et al. 2019 at $z \sim 2$), if this process is efficient, clump feedback could even contribute to the reionization of the Universe (Bouwens et al. 2015).

Recent studies of lensed high-redshift galaxies (e.g. Livermore et al. 2012; Adamo et al. 2013; Johnson et al. 2017; Cava et al. 2018; Meštrić et al. 2022) at higher angular resolution offer the possibility to investigate the substructure of clumps (Meng & Gnedin 2020). At the highest resolution, potential clusters have been detected on scales of a few parsecs (Vanzella et al. 2019, 2021a, b,). One of the challenges for the upcoming James Webb Space Telescope (JWST) and adaptive-optic instruments on the European Extremely Large Telescope (E-ELT) will be the detection of possible high-redshift progenitors of the globular clusters (GCs) observed in the local universe to help solve the many open questions about their origin (e.g. Bastian & Lardo 2018, for a review).

In the context of analyses of clumps on small physical scales, we here present the study of the strongly lensed arc at $z = 1.04$ in Abell 0521 (A521), following the nomenclature in Patrício et al. (2018), we will refer to the galaxy as A521-sys1 in the rest of the paper. With a stellar mass of $M_* = (7.4 \pm 1.2) \times 10^{10}\,\mathrm{M}_\odot$ and a SFR of $(26 \pm 5)\,\mathrm{M}_\odot\,\mathrm{yr}^{-1}$ (Nagy et al. 2021), A521-sys1 can be considered a typical main-sequence star-forming galaxy at $z \sim 1$ (e.g. Speagle et al. 2014). The kinematic analysis reveals a rotation-dominated galaxy typical of systems at cosmic noon with a high-velocity dispersion (Patrício et al. 2018; Girard et al. 2019). In addition, both the molecular gas mass surface density $\Sigma(M_{\rm mol})$, and the SFR surface density Σ(SFR) are elevated by a factor of $\sim$10 compared to local MS galaxies, as expected for high-z gas-rich galaxies. The radial profiles of $\Sigma(M_{\rm mol})$ and Σ(SFR) are very shallow (Nagy et al. 2021), suggesting an intense star-formation activity throughout the entire galaxy, as also indicated by the presence of UV clumps in various subregions of A521-sys1. The gravitational lensing produced by the foreground cluster allows the analysis of A521-sys1 clumps down to scales of few tens of parsecs. In addition, the presence of multiple images of A521-sys1 at different magnification factors allows the comparison of the same clumps seen at different resolution, and hence tests of the effect of resolution on the study of clump populations. This paper is structured as follows: we present the data and the lensing model in Section 2, the analyses including the model used to fit the clumps are described in Section 3. The results are collected in Section 4 (photometric properties of the clumps) and in Section 5 (physical properties of the clumps), followed by their discussion in Section 6. An overall summary of the paper is given in Section 7. Throughout this paper, we adopt a flat Λ-CDM cosmology with $H_0 = 68\,\mathrm{km\,s^{-1}\,Mpc^{-1}}$ and $\Omega_{\rm M} = 0.31$ (Planck Collaboration 2014), and the Kroupa (2001) initial mass function.

2 DATA

2.1 *Hubble Space Telescope* (*HST*)

A521-sys1 was observed with *WFC3/UVIS* in the *F390W* passband with *WFC3/IR* in *F105W* and *F160W* (ID: 15435, PI: Chisholm, exposure times: 2470, 2610, and 5220 s, respectively) with *ACS/WFC* in the *F606W* and *F814W* filters (ID: 16670, PI: Ebeling, exposure times 1200 s). Individual flat-fielded and CTE-corrected exposures were aligned and combined in a single image using the `AstroDrizzle` procedure from the `DrizzlePac` package (Hoffmann et al. 2021), the final images have pixels scales of 0.06 arcsec pixel^{-1}. The astrometry was aligned to the *Gaia* DR2 (Gaia Collaboration 2018). We model the instrumental point-spread function (PSF) from a stack of isolated bright stars within the field of view of the observations. The stack in each filter is fitted with an analytical function described by a combination of Moffat, Gaussian, and 4$^{\rm th}$ degree power-law profiles to mitigate bias introduced by the choice of a specific function. The fit provides a good description of the stacked stars up to a radius of $\sim$20 pixels (corresponding to 1.20 arcsec). The minimum detectable magnitude limit, $\mathrm{mag_{lim}}$ is estimated from the standard deviation σ of the background level in the proximity of A521-sys1, we consider the minimum flux of a PSF light profile whose four brightest pixels are above the 3σ level, similarly to the procedure applied to extract sources (see Section 3.1), this minimum flux is converted to an AB magnitude for each filter. We point out that these values are representative of the depth of the observations in the proximity of A521-sys1, the clumps within this system are observed above the diffuse galaxy background, and their detection limits are discussed in Section 3.2.3. The FWHM values of the PSF, exposure times, zero-points, and depth of the exposures are listed in Table 1.

A521-sys1 appears as a series of multiple distorted images (Fig. 1), in particular, a complete counter-image of A521-sys1 is observed to the north-east of the brightest cluster galaxy (BCG) and two additional, partially lensed images of the galaxy (one mirrored) are observed west and north-west of the BCG. We will refer to these different images of the A521-sys1 galaxy as counter-image (CI), lensed-north (LN), and lensed-south (LS), as showed in the left-hand panel of Fig. 1. The division between LN and LS is traced following the critical line with the help of the lens model described in Section 2.3.

Table 1. Rest-frame pivotal wavelengths (λ_{rest}), exposure times (t_{exp}), AB magnitude zero-points (ZP_{AB}), depth of the observations (mag_{lim}), and FWHM of the PSF (PSF_{FWHM}).

Filter	λ_{rest} (Å)	t_{exp} (s)	ZP_{AB} (mag)	mag_{lim} (mag)	PSF_{FWHM} (arcsec)
WFC3-UVIS-F390W	1920	2470	25.4	27.6	0.097
ACS-WFC-F814W	2900	1200	26.5	27.5	0.112
ACS-WFC-F606W	3940	1200	25.9	27.2	0.116
WFC3-IR-F105W	5160	2610	26.3	27.0	0.220
WFC3-IR-F160W	7520	5220	26.0	26.8	0.237

Black crosses in the left-hand panel of Fig. 1 mark the position of bright foreground or cluster galaxies in the field of view, the relative contribution from such galaxies to the A521-sys1 photometry increases with the wavelength of the respective observation.

On the other hand, they would have a strong effect on the analysis of the clumpiness of A521-sys1, for this reason their flux is subtracted in the latter analysis (see Section 4.2 for more details). Single-band observations are shown in Fig. 2 for *F390W* and in Appendix A for the other filters.

2.2 Ancillary data

A521-sys1 was observed with VLT-MUSE as part of the Multi Unit Spectroscopic Explorer (MUSE) Guaranteed Time Observations (GTO) Lensing Clusters Programme (ID: 100.A-0249, PI: Richard). Observations and data reductions are presented in Patrício et al. (2018). The PSF of MUSE observation is 0.57 arcsec, almost five times larger than the PSF of *HST-F390W*, the reference filter for our clump extraction and analysis, and therefore MUSE data cannot be used for the study of individual clumps. We use MUSE data to estimate the average extinction in radial regions of the galaxy, using the relative strength of nebular emission lines, as described in Appendix E.

ALMA observations of A521-sys1 were acquired during Cycle 4 (ID: 2016.1.00643.S) in band 6, targeting the CO(4-3) emission line, and were presented in Girard et al. (2019) and in Nagy et al. (2021), along with their data reduction analysis. The high resolution of the ALMA observations (beam size: 0.19×0.16 arcsec) allows the study of molecular gas on the same scales as the stellar content, the study of the individual giant molecular clouds (GMCs) is presented in Dessauges-Zavadsky et al. (in preparation).

2.3 Gravitational lens model

The gravitational lens model used in this paper to recover the source properties of the individual clumps was constructed using the LENSTOOL[1] software (Jullo et al. 2007), and is described in detail in Appendix B. Its final Root Mean Square (RMS) accuracy in the image plane, based on the positions of 33 multiple images, is 0.08 arcsec i.e. comparable to the pixel scale of the *HST* data.

The amplification map, showing the magnification factor, μ, associated to each position of A521-sys1 is showed in the right-hand panel of Fig. 1. The magnification factor in the CI region ranges from $\mu \sim 2$–6 with a median of four and a shallow spatial gradient across the image. In LN and LS, magnifications are typically higher (median $\mu \sim 10$) with subregions reaching values $\mu > 20$ for the majority of the arc.

[1] https://projets.lam.fr/projects/lenstool/wiki

3 DATA ANALYSIS

3.1 Clump extraction

We use the *F390W* observations corresponding to rest-frame UV, as reference to extract the clump catalogue. *F390W* is the filter where the clumps are more easily detectable, the galaxy looks less clumpy when moving to longer wavelengths, as also quantitatively shown in the clumpiness analysis of Section 4.2. We use the `SExtractor` software (Bertin & Arnouts 1996) on a portion of the *F390W* data centred on A521-sys1 to extract sources that have a minimum of 4 pixels with $S/N > 3\sigma$ in background-subtracted images. The local background is estimated using a convolution grid of 30 pixels (BACK_SIZE = 30 in the configuration file), smaller grid would result in considering sources as part of the background, and consequently in removing them. Using the galaxy cluster mass model to trace the counter-images of all extracted sources, we notice that one clump (clump '9') is detected in LN but its counter-images in CI and LS are not, the latter being below the detection limits of `SExtractor`, those were therefore added manually to the catalogue. We also search the images in redder filters looking for red clumps that would have missed in the extraction in *F390W*, only one such source is found (clump '4'), lying below the detection limit in *F390W* but bright in all other filters, which is added to the sample. Finally, by a visual inspection we verify that none of the UV clump clearly recognizable by eye is missed by our extraction and we remove foreground galaxies from the catalogue. The final catalogue counts 18 unique clumps. Many of those have multiple images, different images of the same clump have been assigned the same ID number, preceded by the subregion where the image is observed (e.g. 'ci_1', 'ln_1', and 'ls_1' are the same source '1' observed in the counter-image, the lensed-north, and the lensed-south regions, respectively). The cross-identification of various images of the same clump was done with the help of the lens model. In addition, some clumps were divided in multiple subpeaks in the photometric analysis (see Section 3.2.1), each peak was considered as a single entry in the catalogue and we add letters to the ID to differentiate the entries (e.g. clumps 'ci_7a' and 'ci_7b' are two peaks of clump '7'). As consequence, the final catalogue counts 45 entries, spread across the three images of A521-sys1. The position of all clumps on the *F390W* observations is shown in Fig. 2.

3.2 Clump modelling

We modelled the clumps on the image plane, deriving their sizes and magnitudes on the observed data, and later convert those to intrinsic values. We assume that clumps have intrinsic 2D Gaussian profiles in the source plane and that local lensing transformations still result in Gaussian ellipses in the image plane, in order to describe the observed clump light profile we convolve the 2D Gaussian profiles with the instrumental point spread function i.e. the response of the instrument. Asymmetric Gaussian profiles are used to take into account both intrinsic asymmetries in the clump shapes and distortions introduced by the lensing.

We perform the fits in cut-outs of 9×9 pixels, centred on each of the clumps. In order to take into account possible background luminosity in the vicinity of the clumps, we add to the clump model a 1st degree polynomial function, described by three parameters (c_0, c_x, and c_y). The choice of a non-uniform background helps avoiding the contamination to the fit from the tails of nearby bright sources. The 'observable' model, M_f, to be fitted to the data in filter f can be

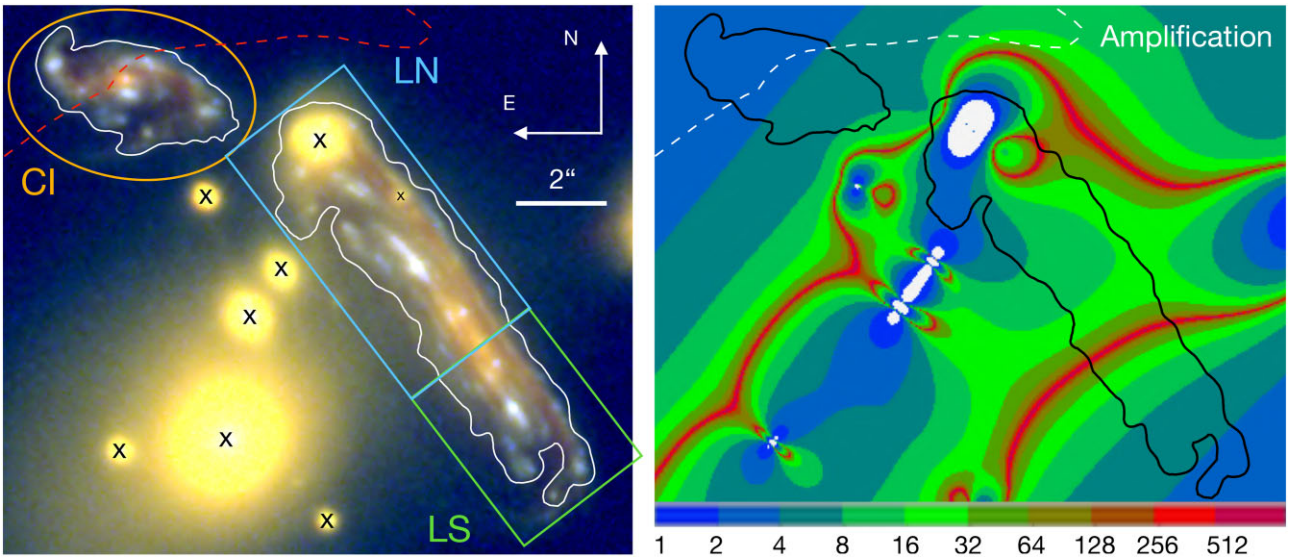

Figure 1. (Left-hand panel): *HST* observations of A521-sys1 (RGB colours are given by *F*160*W*, *F*105*W*, and *F*390*W*, respectively). The division in three subregions discussed in the paper (counter-image CI, lensed-north LN and lensed-south LS) is also shown. Foreground cluster members are marked with an 'x'. (Right-hand panel): amplification map showing the magnification factor, μ, at any position of A521-sys1. A white (black) contour enclosing the galaxy is over-plotted to both panels to make the comparison between them easier. The dashed red (white) line delimits the CI region with multiple images.

therefore summarized as:

$$M_f(x, y|x_0, y_0, F, \sigma_x, axr, \theta, c_0, c_x, c_y) = F \cdot K_f * G_{2D}(x_0, y_0, \sigma_x, axr, \theta) + c_0 + c_x x + c_y y, \quad (1)$$

where K_f parametrizes the PSF in filter f (as described in Section 2.1) and F parametrizes the observed flux (both the PSF and the Gaussian model are normalized). The Gaussian model, G_{2D}, is parametrized by the minor standard deviation σ_x, the axial ratio axr defined by $axr \equiv \sigma_y/\sigma_x > 1$ and the angle θ, using the `astropy.modeling` package, by construction we impose that σ_x refers to the minimum axis of the 2D Gaussian function. The fit is performed using a least-squared method via the `python` package `lmfit` (Newville et al. 2021). We calculate and report 1σ uncertainties derived from the covariance matrix.

Each clump was fitted separately in each of the filters. Due to the clumps being more easily detectable in *F*390*W*, we use the latter as the reference one for determining the clump position and size. As first step, we fit the clumps in *F*390*W*, leaving all parameters free. The *F*390*W* data, along with clump best-fitting models and residuals are shown in Appendix A. For the fit in *F*606*W*, *F*814*W*, *F*105*W*, and *F*160*W*, we keep the resulting values for the clump centre (x_0 and y_0) and its size (σ_x, axr, and θ) as fixed parameters, i.e. we fix the Gaussian shape and its position, leaving free only the flux (and the background parameters). This choice assumes that the source has intrinsically the same shape and size in all bands.

3.2.1 *Fitting together multiple sources*

A variation to the fitting method described above is employed for clumps whose central positions are less than four pixels apart. Due to such closeness the fit of each of the sources would be greatly affected by the other one, bringing unreliable results. For this reason we choose to fit nearby clumps in a single fitting run, by using a larger cut-out of 11 × 11 pixels and modelling two separate gaussians within it, this kind of fit applies only to three pairs of sources. In naming these cases, we use the same numeric ID for the two sources, adding a letter to differentiate them (e.g. clumps 'ci_7a' and 'ci_7b' have been fitted together). In doing so, we are therefore considering the two as separate peaks of the same source, this choice is driven solely by the resolution of our data. An extreme case is clump '9', that, while in the LS image it appears as a single peak, it can be separated into four different subpeaks (plus a separate image) in LN and into three subpeaks in CI. For the fit of its LN representation we choose to fit at the same time all four peaks in a 11 × 11 cut-out, imposing circular symmetry for the sources. This last choice is motivated by the too large number of free parameters if asymmetric profiles were considered. The same approach is used to fit the three peaks in the CI region.

3.2.2 *Minimum resolvable σ_x*

Our fitting method has an intrinsic resolution limit driven mainly by the instrumental PSF, with a *FWHM* equal to 1.6, 1.9, 1.9, 3.7, and 4.0 pixels for *F*390*W*, *F*606*W*, *F*814*W*, *F*105*W*, and *F*160*W*, respectively. The convolution of the PSF with very narrow Gaussian functions will be indistinguishable from the PSF itself. To test what is the minimum size we can resolve, we simulate clumps with various combinations of σ_x and axis ratios, add them on top of the galaxy observations and fit them in the same way we do for the real data. We derive a minimum resolvable size $\sigma_{x,\rm min} = 0.4$ pixel for *F*390*W*. All the sources whose fit results in $\sigma_{\rm x} < 0.4$ pixel will be considered as upper limits in size, as shown in Fig. 3. More details on the process to derive $\sigma_{x,\rm min}$ are given in Appendix C.

3.2.3 *Completeness of the sample*

We test the magnitude completeness of the clump sample by simulating clumps of various magnitudes, including them at random positions on top of the galaxy, and fitting them in the same way as for the real sources. We estimate the completeness limit, $\rm lim_{com}$, as the magnitude above which the fit results become unreliable, using simulated sources of different sizes, $\sigma_x = 0.4$, 1.0, and 2.0 pixels,

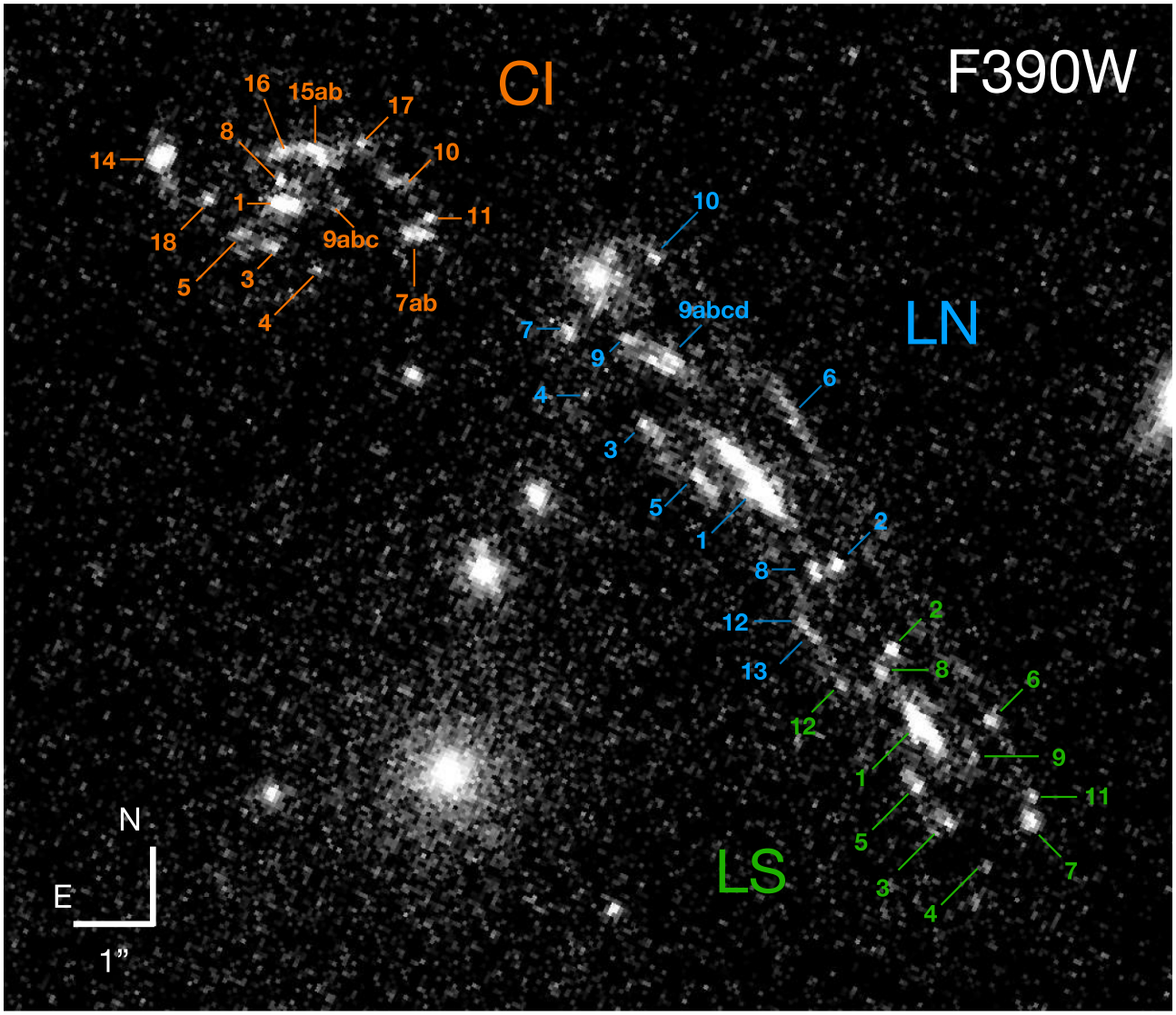

Figure 2. Names and locations of the clumps in A521-sys1 on the *F*390*W* data. The coordinates and main properties of the clump sample are given in Table 3, the complete photometry in all filters is given in Table A1 of Appendix A.

corresponding to 0.024, 0.06, and 0.12 arcsec, respectively. More details on the completeness test are given in Appendix D.

The derived values for *F*390*W* are compared to the photometry of the actual clump sample in Fig. 3, for an easier comparison to clump magnitudes we we corrected $\lim_{com}$ values by the Galaxy reddening in the figure. We find a completeness $\lim_{com} = 27.4$ mag for point-like sources ($\sigma_x \leq 0.4$ pixel), consistent with the faintest unresolved clumps of our sample. This value is only slightly brighter than the minimum detectable magnitude (mag_{lim}) discussed in Section 2.1. The completeness values get brighter for larger sources, namely $\lim_{com} = 26.7$ mag and 25.2 mag for sources with $\sigma_x = 1.0$ pixel (0.06 arcsec) and 2.0 pixels (0.12 arcsec), respectively. These values are still consistent with the faintest clumps we observed at the corresponding sizes and suggest that $\lim_{com}$ traces the magnitudes of the sources which are 3σ above their local background, i.e. the lower limit chosen for extracting the clump catalogue (as seen in Section 3.1).

3.3 Conversion to intrinsic sizes and magnitudes

The fluxes, *F* (in e/s), are converted into observed AB magnitudes by considering the instrumental zero-points relative to each filter (Table 1), the reddening introduced by the Milky Way (0.29, 0.19, 0.11, 0.07, and 0.04 magnitudes for *F*390*W*, *F*606*W*, *F*814*W*, *F*105*W*, and *F*160*W*, respectively) is subtracted in each filter. The photometry of all A521-sys1 clumps is collected in Appendix A for all filters.

In order to convert observed magnitudes into absolute ones we subtract the distance modulus (44.3 mag) and we add the *k* correction, a factor $2.5\log(1+z)$. Concerning the clump sizes measured in *F*390*W*, we calculate the geometrical mean of the minor and major σ derived from the fit, i.e. $\sigma_{xy} \equiv \sqrt{\sigma_x \sigma_y} = \sigma_x \sqrt{axr}$, and we convert it to an effective radius. In the case of the Gaussian function, the effective radius is equivalent to the half-width at half-maximum, $HWHM = FWHM/2$ and therefore $R_{\rm eff}, xy \equiv FWHM/2 = \sigma_{xy}\sqrt{2\ln 2}$. The conversion from pixels to parsec is 1 pixel $\equiv$ 498.5 pc, de-

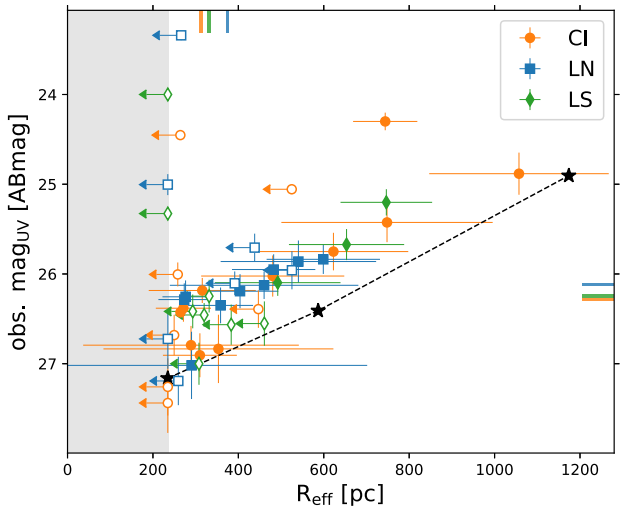

Figure 3. Apparent *F*390*W* magnitudes and sizes of the clumps (colour-coded by the region where they belong) as they appear in the image-frame, i.e. before taking into account the de-lensing. The black stars joint by the dashed line are the completeness limits ($\mathrm{lim_{com}}$) discussed in Section 3.2.3 and Appendix D. The solid line at the top and on the right side of the panel indicate median values for size and magnitudes, respectively. Size upper limits (defined as $\sigma_x < 0.4$ pixel, see Section 3.2.2) are shown as empty markers. The grey area is below the size resolution limit (<235 pc).

rived considering the angular diameter distance of the galaxy of 1713 Mpc and the pixel scale of the observations, 0.06 arcsec pixel^{-1}.

The fitting method and the steps just described return sizes and luminosities as observed in the image plane, i.e. after the effect of the gravitational lensing. In order to recover the intrinsic properties of the clumps, we consider the lensing model, described in detail in Appendix B. First, we focus on the best fit model, resulting in the magnification map shown in Fig. 1 (right-hand panel), for each clump we identify the region enclosed within $R_{\rm eff}$ and use the median amplification value of the selection as the face-value considered for de-lensing sizes and luminosities. We use the standard deviation of the values within the selected region as a first estimate of the uncertainty on the magnification, $\delta\mu_1$. Second, we consider 500 models from the MCMC chain produced with LENSTOOL (Appendix B). These models sample the posterior distribution of each parameter in the mass model of the cluster. For each of those realizations, we re-measure the median amplification value of each clump and use their standard deviation as a measure of the uncertainties related to the best-fitting model, $\delta\mu_2$. We have checked that for each clump the magnification of the best-fitting model is not biased against the median of the distribution of magnifications for the 500 models. We account for both the magnification uncertainty related to the clump extension ($\delta\mu_1$) and the one related to the lens model uncertainties ($\delta\mu_2$) by considering their sum root squared, $\delta\mu = \sqrt{\delta\mu_1^2 + \delta\mu_2^2}$.

Intrinsic luminosities and sizes are derived by dividing the observed quantities by the magnification value and by its square-root, respectively. The final uncertainties combine both photometric and magnification uncertainties via the root sum squared. In this way, they include possible magnification gradients close to the source position's regions with higher magnifications also have a steeper μ gradient, such that the sources within those regions have large uncertainties associated.

Table 2. Models and relative assumptions used in the broad-band SED-fitting process. In all cases spectra from the Yggdrasil stellar population synthesis code (Zackrisson et al. 2011) (based on Starburst99 Padova-AGB tracks), with Kroupa (2001) IMF, are considered.

Model	SFH	Ext. curve	Z
C10 (reference)	Const. SFR (10 Myr)	MW	0.020
SSP	Single burst	MW	0.020
C100	Const. SFR (100 Myr)	MW	0.020
C10-SB	Const. SFR (10 Myr)	Starburst	0.020
C10-008	Const. SFR (10 Myr)	MW	0.008

3.4 Broad-band SED fitting

We use the broad-band photometry to estimate ages and masses of the clumps. The limited number of filters available, covering the rest-frame wavelength range ∼1700–8500 Å, do not allow to fully break the degeneracy between ages and extinctions, nor to constrain the metallicity or the star formation history of the clumps. In order to mitigate the effect of degeneracies, we limit the number of free-parameters making some *a-priori* assumptions. In detail, we use the Yggdrasil stellar population synthesis code (Zackrisson et al. 2011), Yggdrasil models are based on Starburst99 Padova-AGB tracks (Leitherer et al. 1999; Vázquez & Leitherer 2005) with a universal Kroupa (2001) initial mass function (IMF) in the interval 0.1–100 $\mathrm{M_\odot}$. Starburst99 tracks are processed through `Cloudy` software (Ferland et al. 2013) to obtain the evolution of the nebular continuum and line emission produced by the ionized gas surrounding the clumps. Yggdrasil adopts a spherical gas distribution around the emitting source, with hydrogen number density $n_{\rm H} = 10^2$ cm^{-3} and gas filling factor (describing the porosity of the gas) $f_{\rm fill} = 0.01$, typical of H II regions (Kewley & Dopita 2002), and assumes that the gas and the stars form from material of the same metallicity. We choose the models with a gas covering fraction $f_{\rm cov} = 0.5$, i.e. only 50 per centof the Lyman continuum photons produced by the central source ionize the gas, but we point out that our fit results are basically not affected by the choice of $f_{\rm cov}$.

As fiducial model we consider the stellar tracks obtained assuming a continuum star formation for 10 Myr (C10), a Milky Way extinction law (Cardelli, Clayton & Mathis 1989) and Solar metallicity ($Z = 0.02$ as suggested by the analysis in Patrício et al. 2018). The C10 assumption is motivated by most of the clumps in the sample having physical sizes of ∼100 pc. For star-forming regions at larger scales we can expect more complex star formation histories (SFHs) in particular prolonged star-formation events, the opposite is true at smaller scales for stellar clusters and small clumps (few tens of parsecs), where the hypothesis of instantaneous burst ('single stellar population' model, or SSP) is usually assumed. Our clump sample contains sources with a wide range of physical scales (Section 4.1), for this reason, in addition to the fiducial model, we consider a SSP model and a model assuming a continuum star formation for 100 Myr (C100). The comparison between these two 'extreme' assumptions will give the magnitude of the effect of the SFH on the derived properties.

To test the effects of the choice of the extinction curve, we consider a fourth model with the starburst curve (Calzetti et al. 2000) instead of the MW one. Due to the uncertainties associated to the study of stellar metallicity in A521-sys1 in Patrício et al. (2018), we consider a further model, assuming sub-Solar metallicity ($Z = 0.008$). All the models used in the SED-fitting are summarized in Table 2.

Considering the assumptions described above, we are left with three free parameters in our fits, age, mass, and extinction

parametrized by the colour excess $E(B-V)$. The photometric data of our catalogue are fitted to the spectra from the models considered using a minimum-χ^2 technique. Only sources with magnitude uncertainties below 0.6 mag in more than three filters have been fitted. We report in Section 5, the face-values relative to the minimum reduced χ^2 ($\chi^2_{\rm red.,min}$) for each clump, and we assign to it an uncertainty given by the range in properties spanned by the results satisfying the condition $\chi^2_{\rm red.} \leq 1.07$ (consistent with 1σ uncertainties for fits with two degrees of freedom). In cases where the minimum $\chi^2_{\rm red.}$ is above that threshold, we retained within the uncertainty range the values within 10 per cent of $\chi^2_{\rm red.,min}$. The differences in derived properties for each clump given by the choice of the different models of Table 2 are considered and discussed in Section 5.

3.5 Alternative clump selection and photometry

Literature studies offer a variety of methods for extracting clump samples and analysing them. To test the reliability of our extraction and photometric analysis we consider an alternative method: we draw elliptical regions that best follow 3σ contours above the level of the galaxy background to define the clump extent and measure the flux of the clumps within those regions. Such method is used in the analysis on GMC complexes from CO data (e.g Dessauges-Zavadsky et al. 2019; Dessauges-Zavadsky et al., in preparation) but has also been applied to the study of stellar clumps (e.g. Cava et al. 2018). More details on the source extraction, size, and photometry measurements with this alternative method are given in Appendix F, while the derived properties and their differences to the ones of the reference method are discussed in Section 6.2.

4 PHOTOMETRIC RESULTS

4.1 UV sizes and magnitudes of the clumps

We show the distribution of observed sizes and $F390W$ magnitudes of the clumps in Fig. 3. Magnitudes have been considered after correcting for Galactic reddening. We plot apparent sizes, i.e. not corrected for the effect of magnification. The observed magnitudes ranges mostly between 27 and 25 mag (AB system), while sizes are mainly clustered below 600 pc. The minimum size, 235 pc is set by the choice of $\sigma_{\rm x,min} = 0.4$ pixel described in Section 3.2.2 and Appendix C. Many of the clumps observed have upper limits in size, i.e. they show a light profile consistent with the instrumental PSF, at least on their minor axis. We do not observe systematic differences for clumps in different counter-images of the galaxy as can be verified comparing the median sizes and magnitudes reported at the top and on the right side of Fig. 3. In the same figure, we report the completeness limits, $\rm lim_{com}$, derived in Appendix D and discussed in Section 3.2.3, as black stars connected by a dashed line, all sources are above the $\rm lim_{com}$ value or consistent with it.

Absolute UV magnitudes and clump sizes after correcting for the de-lensing are shown in Fig. 4. The values shown are the intrinsic sizes and luminosities of the clumps, also reported in Table 3. De-lensing reveals a wide range of intrinsic properties spanning ∼8 magnitudes and sizes between ∼10 and ∼600 pc. This suggests that we are observing a wide variety of clumps from large star-forming regions on scales of hundreds of parsecs to almost star clusters. The distribution of sizes and magnitudes are summarized in histograms in Fig. 4, while clumps in the CI and LS regions have similar distribution of properties clumps in the LN region are on average smaller and less bright, as suggested by the median values, med($R_{\rm eff}$) = 77, 142, and 156 pc and med($\rm Mag_{UV}$) = −14.5, −15.4, and −15.7 mag for LN, LS, and CI, respectively. Such difference is driven by the large amplification factors reached in some subregions of the LN image and is specifically due to few sources in the LN that thanks to such amplification can be resolved in their subcomponents, four of those sources are the peaks of the same clump '9', already described in Section 3.2.1. We remind that many size measurements return only upper limits affecting the distributions and median values just discussed. Nevertheless, the differences found between median values in CI, LN, and LS remain even when removing clumps with size upper-limits. Some of the brightest and largest sources in the CI are outside the region that produces multiple images (see Fig. 1) and therefore do not have a counterpart either in LN or in LS (black circles in the bottom panel of Fig. 4). Neglecting clumps without multiple images would produce a minimal effect on the median values discussed above. Despite differences in median magnitude and sizes, clumps appear to share similar surface brightnesses between the three subregions, consistent with the conservation of surface brightness by gravitational lensing.

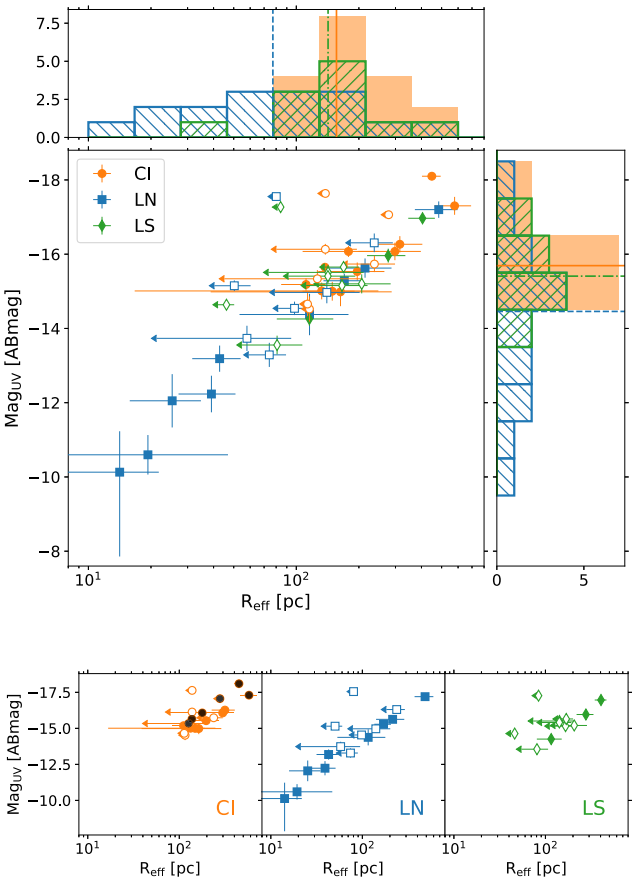

Figure 4. Clumps' de-lensed sizes and absolute $F390W$ magnitudes, colour-coded by the subregion where the clumps are observed (CI, LN, and LS). Size upper limits are shown as empty markers and the length of their arrows reflects the size uncertainty (coming from the uncertainty in the magnification). The top and right histograms show the distributions of sizes and magnitudes in each of the subregions, with solid, dashed and dash–dotted lines giving the median values for CI, LN, and LS, respectively. The bottom panels show separately the sizes and magnitudes of sources in each of the subregions. The black sources in the CI panel (bottom-left) are clumps without a counterpart in either LN or LS.

Table 3. Main intrinsic properties of the clumps in A521-sys1 and relative uncertainties: (1)–(2) RA and Dec coordinates; (3)–(5) magnification factors, effective radii, and absolute UV magnitudes (from *F*390*W*) derived as described in Section 3.2 and Section 3.3 and presented in Section 4.1; (6)–(8) ages, masses, and colour excesses for the reference SSP model (Table 2) derived as described in Section 3.4 and presented in Section 5; (9) mass surface densities, defined as $\langle\Sigma_M\rangle = M/(2\pi R_{\rm eff}^2)$ and discussed in Section 5.1; (10) crossing times, defined as $T_{\rm cr} \equiv 10\sqrt{R_{\rm eff}^3/{\rm GM}}$ and discussed in Section 5.2. Upper and lower limits are indicated by '<' and '>', respectively.

ID	RA [hh:mm:ss]	Dec [hh:mm:ss]	μ	$R_{\rm eff}$ [pc]	Mag$_{\rm UV}$ [AB]	Age [Myr]	log(M) [M$_\odot$]	$E(B-V)$ [mag]	log$\langle\Sigma_M\rangle$ [M$_\odot$pc^{-2}]	$T_{\rm cr}$ [Myr]
(0)	(1)	(2)	(3)	(4)	(5)	(6)	(7)	(8)	(9)	(10)
ci_1	4:54:07.0521	−10:13:16.964	$3.7^{\pm0.2}$	$<138.0^{\pm3.7}$	$-17.6^{\pm0.1}$	4^{+2}_{-3}	$7.38^{+0.11}_{-0.06}$	$0.22^{+0.01}_{-0.04}$	$>2.3^{+0.11}_{-0.06}$	$<1.7^{+0.1}_{-0.3}$
ci_3	4:54:07.0607	−10:13:17.565	$3.9^{\pm0.2}$	$314.8^{\pm89.0}$	$-16.3^{\pm0.2}$	30^{+10}_{-0}	$7.89^{+0.05}_{-0.02}$	$0.18^{+0.01}_{-0.03}$	$2.1^{+0.25}_{-0.25}$	$3.2^{+1.4}_{-1.4}$
ci_4	4:54:07.0179	−10:13:17.879	$4.8^{\pm0.3}$	$132.5^{\pm115.8}$	$-15.0^{\pm0.2}$	11^{+2}_{-3}	$7.64^{+0.08}_{-0.06}$	$0.53^{+0.07}_{-0.09}$	$2.6^{+0.76}_{-0.76}$	$1.2^{+1.5}_{-1.5}$
ci_5	4:54:07.0897	−10:13:17.389	$3.5^{\pm0.2}$	$<237.5^{\pm60.9}$	$-15.7^{\pm0.2}$	50^{+0}_{-0}	$7.28^{+0.00}_{-0.00}$	$0.00^{+0.00}_{-0.00}$	$>1.74^{+0.22}_{-0.22}$	$<4.2^{+1.6}_{-1.6}$
ci_7a	4:54:06.9343	−10:13:17.386	$6.0^{\pm0.5}$	$196.4^{\pm68.9}$	$-15.5^{\pm0.2}$	50^{+50}_{-49}	$7.94^{+0.13}_{-0.50}$	$0.19^{+0.41}_{-0.13}$	$2.55^{+0.33}_{-0.58}$	$1.5^{+0.9}_{-0.8}$
ci_7b	4:54:06.9206	−10:13:17.390	$6.3^{\pm0.5}$	$298.0^{\pm99.3}$	$-16.1^{\pm0.2}$	11^{+69}_{-10}	$7.28^{+0.54}_{-0.09}$	$0.31^{+0.16}_{-0.31}$	$1.53^{+0.61}_{-0.3}$	$6.0^{+3.0}_{-8.0}$
ci_8	4:54:07.0529	−10:13:16.650	$3.5^{\pm0.2}$	$<138.0^{\pm57.7}$	$-16.1^{\pm0.1}$	20^{+0}_{-5}	$8.29^{+0.07}_{-0.28}$	$0.47^{+0.06}_{-0.04}$	$>3.21^{+0.37}_{-0.46}$	$<0.6^{+0.4}_{-0.4}$
ci_9a	4:54:07.0006	−10:13:16.819	$4.1^{\pm0.2}$	$<115.7^{\pm3.3}$	$-14.5^{\pm0.3}$	15^{+5}_{-1}	$6.91^{+0.34}_{-0.13}$	$0.41^{+0.08}_{-0.09}$	$>1.98^{+0.34}_{-0.13}$	$<2.2^{+0.3}_{-1.3}$
ci_9b	4:54:06.9922	−10:13:16.951	$4.3^{\pm0.3}$	$148.9^{\pm41.8}$	$-15.0^{\pm0.3}$	50^{+0}_{-10}	$6.89^{+0.04}_{-0.02}$	$0.00^{+0.05}_{-0.00}$	$1.75^{+0.25}_{-0.24}$	$3.3^{+1.4}_{-1.4}$
ci_9c	4:54:07.0007	−10:13:17.050	$4.3^{\pm0.3}$	$<113.3^{\pm3.4}$	$-14.7^{\pm0.3}$	60^{+40}_{-10}	$7.06^{+0.20}_{-0.05}$	$0.00^{+0.04}_{-0.00}$	$>2.15^{+0.2}_{-0.06}$	$<1.8^{+0.1}_{-0.5}$
ci_10	4:54:06.9492	−10:13:16.684	$4.7^{\pm0.3}$	$163.2^{\pm124.4}$	$-15.0^{\pm0.4}$	14^{+26}_{-5}	$7.36^{+0.54}_{-0.08}$	$0.40^{+0.17}_{-0.15}$	$2.14^{+0.86}_{-0.67}$	$2.2^{+2.5}_{-3.7}$
ci_11	4:54:06.9141	−10:13:17.163	$5.9^{\pm0.4}$	$111.4^{\pm26.8}$	$-15.2^{\pm0.2}$	12^{+18}_{-11}	$6.84^{+0.47}_{-0.08}$	$0.26^{+0.14}_{-0.18}$	$1.95^{+0.52}_{-0.22}$	$2.3^{+0.8}_{-2.4}$
ci_14	4:54:07.1624	−10:13:16.335	$2.7^{\pm0.1}$	$448.6^{\pm46.3}$	$-18.1^{\pm0.1}$	40^{+0}_{-27}	$8.61^{+0.04}_{-0.47}$	$0.13^{+0.15}_{-0.02}$	$2.5^{+0.1}_{-0.48}$	$2.4^{+0.9}_{-0.4}$
ci_15a	4:54:07.0211	−10:13:16.236	$3.6^{\pm0.2}$	$<278.1^{\pm7.3}$	$-17.1^{\pm0.1}$	5^{+2}_{-1}	$7.76^{+0.02}_{-0.08}$	$0.40^{+0.01}_{-0.05}$	$>2.08^{+0.03}_{-0.09}$	$<3.1^{+0.3}_{-0.1}$
ci_15b	4:54:07.0140	−10:13:16.392	$3.7^{\pm0.2}$	$137.3^{\pm3.6}$	$-15.6^{\pm0.1}$	20^{+0}_{-0}	$7.73^{+0.02}_{-0.04}$	$0.31^{+0.01}_{-0.02}$	$2.66^{+0.03}_{-0.04}$	$1.1^{+0.1}_{-0.1}$
ci_16	4:54:07.0497	−10:13:16.259	$3.4^{\pm0.2}$	$577.3^{\pm115.7}$	$-17.3^{\pm0.2}$	60^{+0}_{-0}	$8.14^{+0.02}_{-0.00}$	$0.00^{+0.01}_{-0.00}$	$1.82^{+0.18}_{-0.17}$	$6.0^{+1.8}_{-1.8}$
ci_17	4:54:06.9778	−10:13:16.144	$3.9^{\pm0.2}$	$<126.3^{\pm81.2}$	$-15.3^{\pm0.2}$	4^{+2}_{-1}	$6.76^{+0.08}_{-0.09}$	$0.27^{+0.04}_{-0.06}$	$>1.76^{+0.56}_{-0.57}$	$<3.0^{+2.9}_{-2.9}$
ci_18	4:54:07.1194	−10:13:16.912	$3.1^{\pm0.1}$	$178.2^{\pm70.9}$	$-16.1^{\pm0.1}$	20^{+0}_{-8}	$7.76^{+0.02}_{-0.27}$	$0.24^{+0.12}_{-0.01}$	$2.46^{+0.35}_{-0.44}$	$1.6^{+1.0}_{-0.9}$
ln_1	4:54:06.6065	−10:13:20.897	$11.0^{\pm0.8}$	$<80.1^{\pm2.8}$	$-17.6^{\pm0.1}$	11^{+1}_{-2}	$7.12^{+0.06}_{-0.06}$	$0.07^{+0.04}_{-0.05}$	$>2.52^{+0.07}_{-0.07}$	$<1.0^{+0.1}_{-0.1}$
ln_2	4:54:06.5362	−10:13:21.911	$21.8^{\pm1.6}$	$<50.3^{\pm9.9}$	$-15.2^{\pm0.1}$	11^{+1}_{-1}	$6.58^{+0.04}_{-0.03}$	$0.19^{+0.03}_{-0.04}$	$>2.38^{+0.18}_{-0.17}$	$<0.9^{+0.3}_{-0.3}$
ln_3	4:54:06.7141	−10:13:20.003	$6.4^{\pm0.6}$	$214.1^{\pm72.9}$	$-15.6^{\pm0.3}$	7^{+93}_{-6}	$7.48^{+0.54}_{-0.11}$	$0.47^{+0.13}_{-0.42}$	$2.02^{+0.61}_{-0.32}$	$2.9^{+1.5}_{-3.8}$
ln_4	4:54:06.7692	−10:13:19.588	$3.4^{\pm0.4}$	$<140.2^{\pm61.4}$	$-15.0^{\pm0.3}$	10^{+30}_{-9}	$7.61^{+0.45}_{-0.12}$	$0.55^{+0.16}_{-0.28}$	$>2.52^{+0.59}_{-0.4}$	$<1.3^{+0.9}_{-1.5}$
ln_5	4:54:06.6649	−10:13:20.718	$8.0^{\pm0.7}$	$170.2^{\pm35.1}$	$-15.3^{\pm0.2}$	40^{+20}_{-32}	$7.15^{+0.09}_{-0.53}$	$0.03^{+0.27}_{-0.03}$	$1.89^{+0.2}_{-0.56}$	$3.0^{+1.4}_{-1.0}$
ln_6	4:54:06.5781	−10:13:19.957	$16.5^{\pm1.0}$	$<57.9^{\pm36.6}$	$-13.7^{\pm0.3}$	4^{+1}_{-1}	$6.40^{+0.06}_{-0.06}$	$0.37^{+0.03}_{-0.04}$	$>2.07^{+0.55}_{-0.55}$	$<1.4^{+1.3}_{-1.3}$
ln_7	4:54:06.7850	−10:13:18.739	$1.5^{\pm0.2}$	$484.2^{\pm112.4}$	$-17.2^{\pm0.2}$	1^{+99}_{-0}	$8.07^{+0.40}_{-0.31}$	$0.46^{+0.05}_{-0.46}$	$1.91^{+0.44}_{-0.37}$	$5.0^{+2.1}_{-4.1}$
ln_8	4:54:06.5573	−10:13:22.002	$20.0^{\pm1.7}$	$<98.1^{\pm16.2}$	$-14.5^{\pm0.2}$	15^{+15}_{-4}	$7.02^{+0.47}_{-0.07}$	$0.31^{+0.13}_{-0.10}$	$>2.24^{+0.49}_{-0.16}$	$<1.5^{+0.4}_{-1.5}$
ln_9	4:54:06.7297	−10:13:18.834	$15.8^{\pm7.8}$	$115.8^{\pm62.5}$	$-14.4^{\pm0.6}$	90^{+110}_{-89}	$7.17^{+0.40}_{-0.83}$	$0.01^{+0.56}_{-0.01}$	$2.25^{+0.62}_{-0.95}$	$1.6^{+1.5}_{-1.8}$
ln_9a	4:54:06.6850	−10:13:19.162	$119.4^{\pm76.4}$	$25.3^{\pm9.5}$	$-12.1^{\pm0.7}$	–	–	–	–	–
ln_9b	4:54:06.6938	−10:13:19.247	$40.8^{\pm11.4}$	$42.8^{\pm11.2}$	$-13.2^{\pm0.4}$	7^{+93}_{-6}	$6.39^{+0.66}_{-0.21}$	$0.43^{+0.17}_{-0.43}$	$2.33^{+0.7}_{-0.31}$	$0.9^{+0.4}_{-1.7}$
ln_9c	4:54:06.7074	−10:13:19.115	$106.9^{\pm44.8}$	$39.1^{\pm11.9}$	$-12.2^{\pm0.5}$	50^{+252}_{-49}	$6.82^{+0.44}_{-0.73}$	$0.26^{+0.50}_{-0.26}$	$2.84^{+0.52}_{-0.78}$	$0.5^{+0.3}_{-0.5}$
ln_9d	4:54:06.6937	−10:13:19.053	$642.4^{+1338.6}_{-641.4}$	$14.1^{+15.0}_{-14.1}$	$-10.1^{+2.3}_{-1.1}$	–	–	–	–	–
ln_10	4:54:06.7057	−10:13:17.705	$2.7^{\pm0.5}$	$<237.1^{\pm54.2}$	$-16.3^{\pm0.3}$	1^{+89}_{-0}	$7.49^{+0.44}_{-0.33}$	$0.39^{+0.07}_{-0.39}$	$>1.95^{+0.48}_{-0.38}$	$<3.3^{+1.4}_{-3.1}$
ln_12	4:54:06.5671	−10:13:22.744	$50.2^{\pm11.4}$	$<74.2^{\pm15.1}$	$-13.3^{\pm0.3}$	3^{+7}_{-2}	$6.07^{+0.24}_{-0.16}$	$0.34^{+0.07}_{-0.10}$	$>1.53^{+0.3}_{-0.24}$	$<3.0^{+1.0}_{-1.4}$
ln_13	4:54:06.5553	−10:13:22.927	$225.6^{\pm78.5}$	$19.3^{+27.6}_{-19.3}$	$-10.6^{\pm0.5}$	–	–	–	–	–
ls_1	4:54:06.4604	−10:13:24.085	$7.8^{\pm0.5}$	$<84.1^{\pm2.9}$	$-17.3^{\pm0.1}$	5^{+1}_{-2}	$7.18^{+0.04}_{-0.03}$	$0.19^{+0.03}_{-0.02}$	$>2.53^{+0.05}_{-0.04}$	$<1.0^{+0.1}_{-0.1}$
ls_2	4:54:06.4853	−10:13:23.066	$25.9^{\pm2.5}$	$<46.1^{\pm4.1}$	$-14.6^{\pm0.1}$	3^{+1}_{-1}	$6.61^{+0.07}_{-0.04}$	$0.34^{+0.02}_{-0.02}$	$>2.48^{+0.11}_{-0.09}$	$<0.8^{+0.1}_{-0.1}$
ls_3	4:54:06.4322	−10:13:25.466	$4.3^{\pm0.3}$	$<142.2^{\pm68.6}$	$-15.5^{\pm0.2}$	12^{+1}_{-0}	$7.39^{+0.02}_{-0.04}$	$0.38^{+0.01}_{-0.06}$	$>2.29^{+0.42}_{-0.42}$	$<1.7^{+1.3}_{-1.3}$
ls_4	4:54:06.3976	−10:13:26.049	$3.4^{\pm0.2}$	$<165.8^{\pm54.3}$	$-15.2^{\pm0.2}$	8^{+32}_{-7}	$7.71^{+0.41}_{-0.07}$	$0.58^{+0.14}_{-0.30}$	$>2.48^{+0.5}_{-0.29}$	$<1.5^{+0.7}_{-1.4}$
ls_5	4:54:06.4618	−10:13:24.964	$5.5^{\pm0.4}$	$<142.0^{\pm50.2}$	$-15.4^{\pm0.2}$	40^{+20}_{-32}	$7.20^{+0.08}_{-0.54}$	$0.03^{+0.26}_{-0.03}$	$>2.1^{+0.32}_{-0.62}$	$<2.1^{+1.4}_{-1.2}$
ls_6	4:54:06.3934	−10:13:24.044	$5.6^{\pm0.4}$	$276.8^{\pm57.9}$	$-16.0^{\pm0.2}$	40^{+50}_{-33}	$7.71^{+0.13}_{-0.51}$	$0.11^{+0.29}_{-0.10}$	$2.03^{+0.22}_{-0.54}$	$3.3^{+1.5}_{-1.2}$
ls_7	4:54:06.3565	−10:13:25.426	$3.4^{\pm0.2}$	$404.7^{\pm59.2}$	$-17.0^{\pm0.2}$	50^{+50}_{-10}	$8.28^{+0.14}_{-0.05}$	$0.13^{+0.05}_{-0.12}$	$2.27^{+0.19}_{-0.14}$	$3.0^{+0.7}_{-0.9}$
ls_8	4:54:06.4956	−10:13:23.390	$18.1^{\pm1.9}$	$115.6^{\pm35.0}$	$-14.3^{\pm0.2}$	12^{+1}_{-2}	$7.12^{+0.03}_{-0.04}$	$0.45^{+0.05}_{-0.05}$	$2.19^{+0.27}_{-0.27}$	$1.7^{+0.8}_{-0.8}$
ls_9	4:54:06.4098	−10:13:24.546	$5.0^{\pm0.3}$	$<206.4^{\pm78.0}$	$-15.2^{\pm0.3}$	5^{+2}_{-1}	$6.98^{+0.03}_{-0.10}$	$0.38^{+0.03}_{-0.06}$	$>1.55^{+0.33}_{-0.34}$	$<4.9^{+2.8}_{-2.8}$
ls_11	4:54:06.3552	−10:13:25.084	$3.6^{\pm0.2}$	$<168.8^{\pm31.7}$	$-15.7^{\pm0.1}$	13^{+1}_{-1}	$7.20^{+0.02}_{-0.02}$	$0.28^{+0.04}_{-0.04}$	$>1.94^{+0.16}_{-0.16}$	$<2.8^{+0.8}_{-0.8}$
ls_12	4:54:06.5318	−10:13:23.573	$22.5^{\pm2.4}$	$<80.8^{\pm26.1}$	$-13.6^{\pm0.3}$	3^{+3}_{-2}	$5.91^{+0.14}_{-0.12}$	$0.26^{+0.03}_{-0.05}$	$>1.3^{+0.31}_{-0.3}$	$<4.1^{+2.0}_{-2.1}$

4.2 Clumpiness

We measure the clumpiness of A521-sys1 in its three subregions for each filter, we consider clumpiness as the fraction of the galaxy luminosity coming from clumps with respect to the total luminosity of the galaxy. This definition was already used in literature (e.g. Messa et al. 2019) and in high-redshift galaxies has been used also as a proxy for the cluster formation efficiency (Vanzella et al. 2021b). To avoid contamination from nearby cluster members, we subtract them out of the observations using the `Ellipse` class in the `photutils python` library, providing the tools for an elliptical isophote analysis (following the methods described by Jedrzejewski 1987). Such subtraction was not needed in the *F*390*W* filter at the redshift of A521-sys1 this filter corresponds to rest-frame FUV regime and therefore we do not expect significant contamination, as confirmed by visual inspection. The orange ellipse and blue and green boxes in Fig. 1 (left-hand panel) mark the regions of the galaxy included in the extraction of the total flux of the system. These contours are driven by ensuring that all the extracted clumps lie within the area and are the same for all filters. We check that increasing the area covered by these regions we would add <5 per cent of the galaxy flux, while including mostly local background emission. In order to exclude the contribution of local background from the measure of the galaxy flux, we perform aperture photometry in the aforementioned elliptical and rectangular regions employing an annular sky region with a width of 0.3 arcsec (5 pixels) around each of the three apertures. A foreground galaxy is located on top of the northern part of the LN image. Despite the subtraction of the galaxy, some residuals remains and for this reason a small circular region covering the galaxy is excluded from the flux measurement. Since we are interested in measuring the source-plane flux of the galaxy, the nearby region within the close critical line (in red in the magnification map of the right-hand panel of Fig. 1), corresponding to the position of the clumps ln_9a, b, c, d, is also excluded, as it represent a further multiple image of a fraction of the A521-sys1 galaxy.

The source-plane flux of each of the subregions is calculated by dividing the observed flux by its magnification, on a pixel-by-pixel basis. The de-lensed flux of clumps is calculated by dividing the clump photometry by the amplification factor assigned to it, as already described in Section 3.3. The ratios of these two measurements, for each filter and in each subregion, give the clumpiness values, reported in Fig. 5.

The main trend observed is that clumpiness is high in the UV and decreases when moving to longer wavelength. This trend confirms what can be noticed from the single-band observations collected in Appendix A, i.e. the galaxy has a less clumpy appearance at redder wavelengths. The clumpiness in *F*390*W* tracing rest-frame UV wavelengths (∼1900 Å) and therefore the massive stars from recent star-formation suggests that a considerable fraction (20−50 per cent) of recent star formation is taking place in the observed clumps. Redder wavelengths trace older population of stars distributed along the entire galaxy. The clumpiness measurement for the LN subregion is lower than the ones for CI and LS, though 2σ consistent in the bluest band. We attribute this difference mainly to the presence of residuals from the foreground galaxy in the north part of LN. This is confirmed by a second measure of the clumpiness in LN done by excluding the northern part of the subregion (the one encompassing the clumps ln_4, ln_7, ln_9, and ln_10) this further measure is plotted as empty blue markers in Fig. 5. A second cause to this difference could be the lower average physical resolution reached in CI and LS, compared to LN, as literature studies have shown how low-clump resolutions lead to over-estimate their contribution to the galaxy luminosity (Tamburello et al. 2017; Messa et al. 2019).

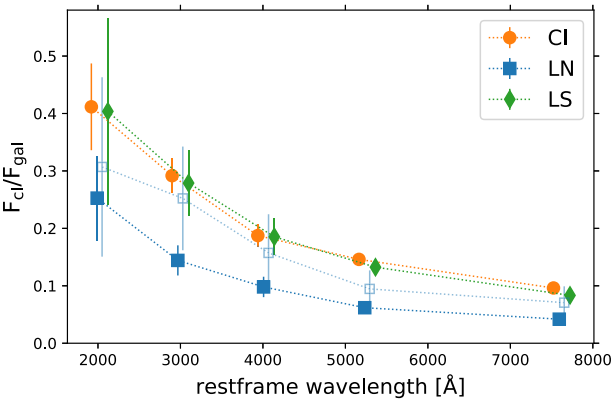

Figure 5. Clumpiness measured as the ratio of the galaxy luminosity coming from clumps in function of the rest-frame wavelengths for filters *F*390*W*, *F*606*W*, *F*814*W*, *F*105*W*, and *F*160*W* from left to right for the three images of A521-sys1 (orange circles for CI, blue squares for LN, and green diamonds for LS). The clumpiness is measured using de-lensed galaxy and clump fluxes and therefore represent the source-plane value. The empty blue squares represent an alternative measure carried out excluding the northern part of the LN subregion, possibly contaminated by the residual of a bright foreground galaxy. A small shift to the values on the *x*-axis have been applied for clarity of the plot, even though the same wavelengths are observed in CI, LN, and LS.

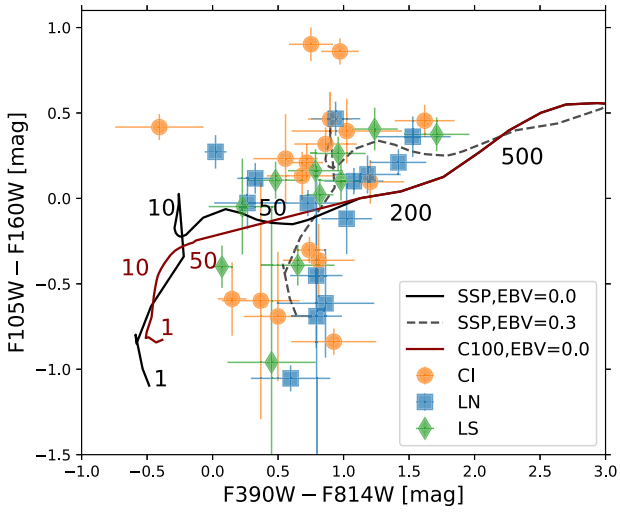

Figure 6. Colour–colour diagram of the clumps, with $UV-B$ and $V-I$ colours on *x* and *y*-axis, respectively. Over-imposed are the stellar track from the SSP and C100 models used for the SED fitting, as black and dark-red solid lines, respectively. The colours at the ages of 1, 10, 50, 200, and 500 Myr, are marked. The colours at 200 and 500 Myr are the same for the two models. The black dashed line show the SSP track at an extinction of $E(B-V) = 0.3$ mag (assuming Milky Way curve).

4.3 Colour–colour diagrams

Colour–colour diagrams provide an intuitive way of estimating the age range covered by the clumps in our sample. In particular, we focus in Fig. 6 on the colours given by the filters *F*390*W*–*F*814*W* (on the *x*-axis) and *F*105*W*–*F*160*W* (on the *y*-axis), because of the rest-frame wavelengths probed by these filters (∼2000, ∼4000, ∼5300,

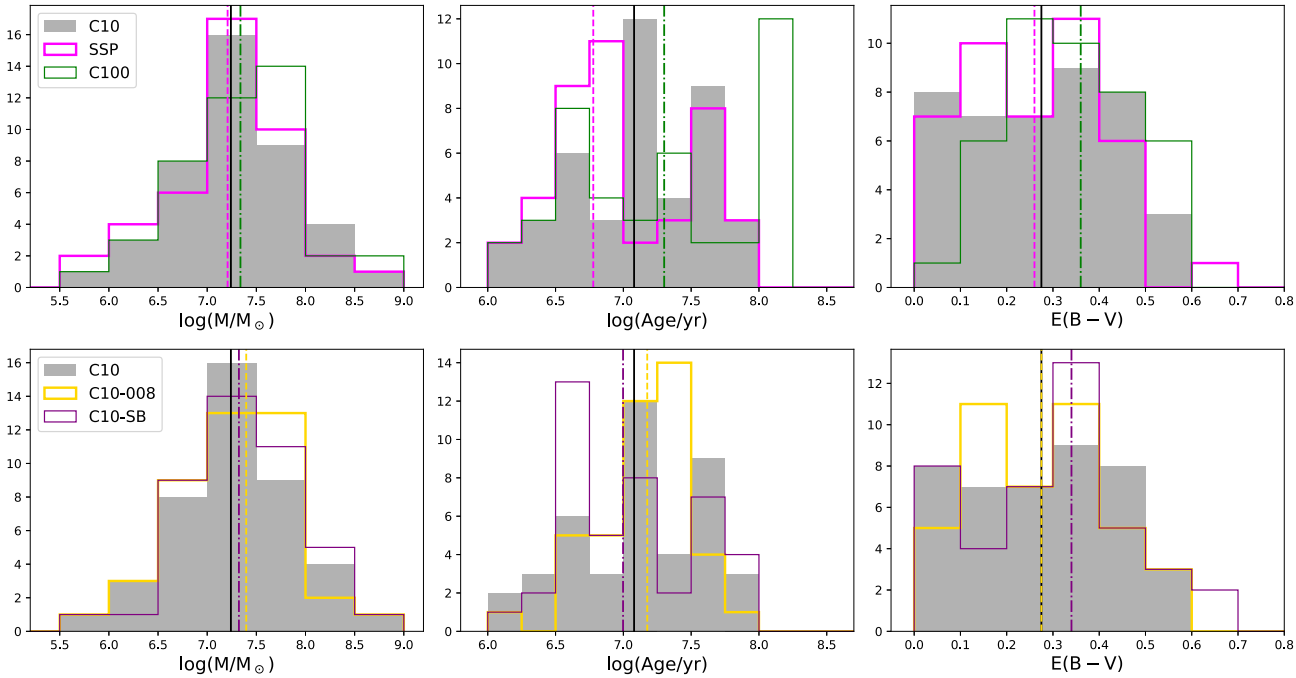

Figure 7. Distributions of masses (left-hand panels), ages (central panels), and colour-excesses (right-hand panels) for all the SED models listed in Table 2. Vertical lines give the median value for each of the distributions. The 100 Myr continuum SF model (C100) gives on average the oldest ages, highest masses, and highest extinctions. The instantaneous burst (SSP) gives the youngest ages but masses and extinctions similar to the reference C10 model. The assumption of either a Calzetti et al. 2000 extinction curve (C10-SB) or a lower metallicity model (C10-008) has on average a small effect on the derived properties. The clump masses are much less sensitive than ages to the model assumption and remain overall stable within ∼0.2 dex.

and ∼7700 Å) we call these colours $UV - B$ (x-axis) and $V - I$ (y-axis), although no conversion to the Johnson filter system is applied. We over-plot on such a diagram, the stellar evolution tracks used for the broad-band SED fitting (described in Section 3.4), and in particular the SSP and C100 tracks, i.e. the two extreme cases of SFH considered. We notice that they show similar behaviours with the $UV - B$ colour remaining almost constant for ages 1–10 Myr and then changing by ∼3 magnitudes for ages 10–500 Myr, the opposite is true for the $V - I$ colour, that changes by 1 mag in the first 10 Myr and then remains almost constant for the rest of the stellar evolution. Extinction moves the curve towards redder colour and therefore specifically towards the top-right of the diagram in Fig. 6. The colours of our clump sample are scattered by ∼1.5 mag on both x and y-axes. They all fall in the age range ∼10–200 Myr, if the no-extinction tracks are considered. However, while their scatter in the $UV - B$ colour can be due to a spread in ages in the range 10–200 Myr, the large spread in $V - I$ suggests the presence of some extinction and of younger ages (1–10 Myr). In particular, data-points seem to be well aligned along the track with an extinction of $E(B - V) = 0.3$ mag.

5 RESULTS OF BROAD-BAND SED FITTING

Individual values for the derived masses, ages, and extinctions in the case of our reference (SSP) model are collected in Table 3, their distributions are shown in Fig. 7. Three clumps have detections in less than four filters and therefore were not fitted. Masses range mainly between $10^6$and 10^8 M$_\odot$, but extends up to ∼10^9 M$_\odot$, ages are distributed between 1 and 100 Myr with the majority of clumps resulting younger than 20 Myr. Extinctions range between $E(B - V) = 0.0$ mag and $E(B - V) = 0.6$ mag with a peak around $E(B - V) \sim 0.3$ mag.

As discussed in Section 3.4, the limited number of filters available implies taking assumptions on the models to be adopted. We show in Fig. 7, the distribution of derived properties using the combination of assumptions listed in Table 2 to help unveiling possible biases associated to the choice of stellar models.

The assumption of longer star formation histories (C100) produce older derived ages on average (as already pointed out in the literature, e.g. Adamo et al. 2013), and the opposite is true for instantaneous burst of star formation (SSP), ages derived using our reference model, C10, are on average in-between (top panel of Fig. 7). We point out that the difference in median ages for those three models is only ∼10 Myr, the main difference is the presence of a considerable fraction of sources (almost one third of the sample) with ages $\gtrsim$100 Myr in the case of C100. The C100 model also produces on average larger masses (by only ∼0.10 dex) and higher extinctions (by ∼0.1 mag). Smaller difference are observed if either a lower metallicity (C10-008) or a difference extinction curve (C10-SB) are assumed (bottom panel of Fig. 7). Overall, we notice that the distribution of ages is the one most affected by the model assumptions, while the distribution of derived masses is similar in all cases. We point out that the lowest median $\chi^2_{\rm red.}$ value is found considering the reference C10 model is considered. We find four sources of the sample (ci_8, ci_9a, ci_15b, ln_1) whose SED fit with the SSP model gives a much lower $\chi^2_{\rm red.}$ than with our reference one, the difference in derived properties with the two models is however negligible.

The distributions just discussed only show the best-fitting values and are associated in some cases to large uncertainties. The uncertainties within the reference model range to ∼0.5, 1.0, and 0.3 mag for log(M), log(Age) and $E(B - V)$, respectively, but their

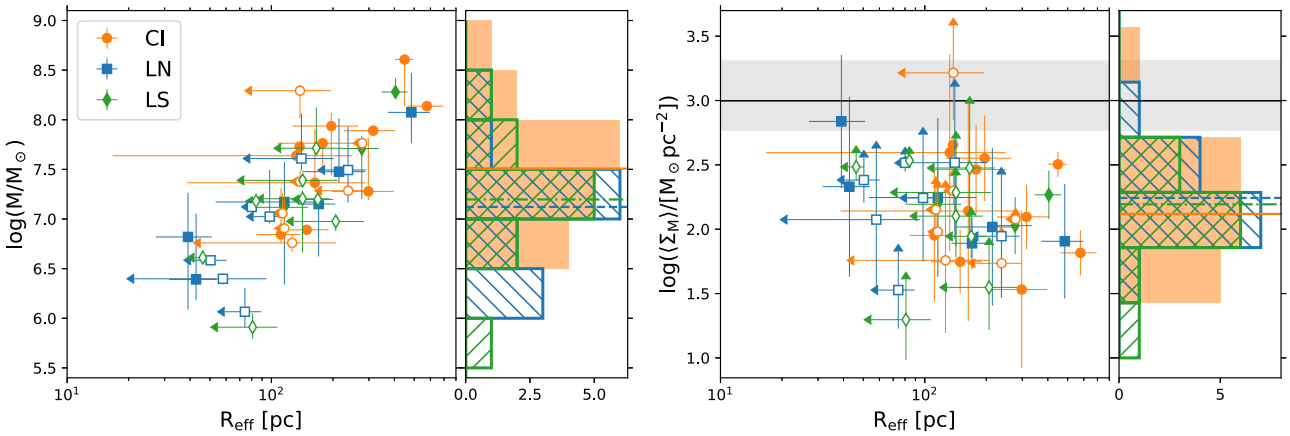

Figure 8. Size versus $\log(M/\mathrm{M}_\odot)$ (left-hand panel) and mass surface density (right-hand panel). Sources are colour-coded according to the subregion where the clumps are observed. Size upper limits are shown as empty markers and the length of their arrows reflects the size uncertainty. Empty markers in the right plot are upper limits on the size and as consequence, lower limits on the density. Each panel has a box showing the distribution of $\log(M/\mathrm{M}_\odot)$ and mass density in each of the subregions of A521-sys1. The black horizontal line (and the grey shaded area) in the right-hand panel represent the typical surface density of a nearby massive cluster (and the uncertainty associated) with $M = 10^5\,\mathrm{M}_\odot$ and $R_{\rm eff} = 4\,\mathrm{pc}$ (Brown & Gnedin 2021). Three clumps do not have derived masses due to the lack of enough filter detections (see Section 5 and Table 3) and therefore are not shown in the plots.

distributions are mainly distributed around zero. The difference in derived properties caused by the choice of different models are mostly consistent with the intrinsic uncertainty within the single model.

5.1 Masses and densities

We compare the derived masses to the sizes of the clumps in Fig. 8 (left-hand panel). As pointed out in the previous paragraph, the range of masses spans more than two orders of magnitude, this range is similar in all three images of A521-sys1, and difference in the median mass is ∼0.4 dex between clumps in the LN field (less massive) and the ones in CI. We observe quite large scatters in mass ($\gtrsim$0.5 dex) at any given clump size but also a robust correlation between mass and size (Spearman's coefficient: 0.78, p-value: 10^{-9}), probably driven by incompleteness effects, as low-mass large clumps will fall below our detection limits. By combining masses and sizes, we study the clump average mass density. We choose to focus on the surface densities instead of the volume ones because in many cases we are dealing with star-forming regions of hundreds of parsecs in size and we do not know their 3D intrinsic shape, therefore we cannot assume spherical symmetries. We define $\langle\Sigma_M\rangle = M/(2\pi\,R_{\rm eff}^2)$[2] and plot the derived values in Fig. 8 (right-hand panel). They span ∼2 orders of magnitude in the range 10–1000 $\mathrm{M}_\odot\,\mathrm{pc}^{-2}$. We observe only a weak anti-correlation between clump size and surface density (Spearman's $\rho_s = -0.3$, *p-val*: 0.06). There is not a significant density difference for clumps in different fields, with a 0.12 dex difference between LN (denser clumps) and CI. For comparison, a typical low-redshift young massive star cluster of $10^5\,\mathrm{M}_\odot$ has a median size of 4 pc (Brown & Gnedin 2021) and therefore a typical surface density of $10^3\,\mathrm{M}_\odot\,\mathrm{pc}^{-2}$, this value shown as a black solid line on the right-hand panel of Fig. 8 is almost one order of magnitude larger than the median values found for our sample, but we remind that a good fraction of our measurements are upper limits in size and therefore lower limit in terms of mass density. Two clumps have $\langle\Sigma_M\rangle$ values comparable to the one of local massive clusters, namely one of the subpeaks of clump ln_9 and ci_8. The latter displays a large-mass density despite being observed at scales >10 times larger in size than local massive clusters and is discussed in more detail in Section 6.4.

5.2 Age distributions

Fig. 7 suggests that the bulk of clumps in A521-sys1 has ages close to ∼10 Myr with a few possibly as old as ∼100 Myr. This picture does not drastically change when considering age uncertainties and other stellar models, we observe that all clumps have derived ages <200 Myr, and the majority of them <100 Myr. The derived age distribution is therefore consistent with clumps being clearly detected in F390W, covering rest-frame 2000 Å UV emission associated to young stars. Taking 100 Myr as an upper limit on the age of the clumps (as suggested by our reference C10 model), we estimate SFRs of individual clumps, the derived values span the range 0.008–4 $\mathrm{M}_\odot\,\mathrm{yr}^{-1}$ consistent with the range covered by UV magnitudes, if those are converted to SFR values using the factor from Kennicutt & Evans (2012) (see also Section 6.1 and Fig. 10). Summing the contributions from all clumps we obtain 12.4, 2.9, and 3.9 $\mathrm{M}_\odot\,\mathrm{yr}^{-1}$ in CI, LN, and LS, respectively. Compared to the total SFR of the galaxy, ∼16 $\mathrm{M}_\odot\,\mathrm{yr}^{-1}$ (Nagy et al. 2021)[3] clumps appear to represent a good fraction of the galaxy current SFR, as already suggested by the clumpiness analysis in Section 3.2.3. We remind that the clump SFR values just derived are based over an age range of 100 Myr and therefore constitute lower limits, larger values (by a factor ∼10) would result from taking the best-fitting individual clump ages, suggesting an increase in the very recent SF activity of A521-sys1.

Clump ages can be compared to their crossing time, which in terms of empirical parameters can be found as:

$$T_{\rm cr} \equiv 10\left(\frac{R_{\rm eff}^3}{\mathrm{GM}}\right)^{1/2} \qquad (2)$$

[2]The factor 2 at denominator is driven by $R_{\rm eff}$ being defined as the radius enclosing half of the source mass.

[3]The original value SFR = 26 $\mathrm{M}_\odot\,\mathrm{yr}^{-1}$ reported in Nagy et al. (2021) was derived assuming a Salpeter (1955) IMF and is here converted to match the assumption of Kroupa (2001) IMF used to derive clump masses.

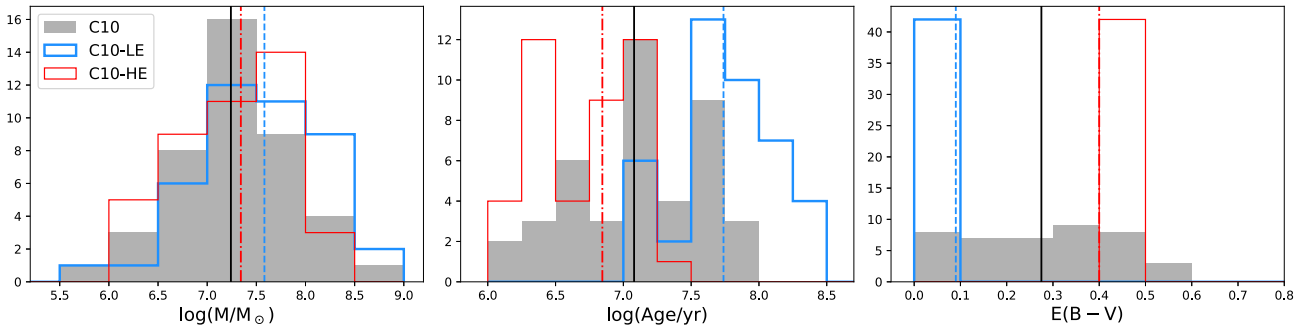

Figure 9. Distributions of masses (left-hand panels), ages (central panels), and colour-excesses (right-hand panels) for the low-extinction (C10-LE) and high-extinction (C10-HE) models, compared to the reference C10 model. Vertical lines give the median value for each of the distributions.

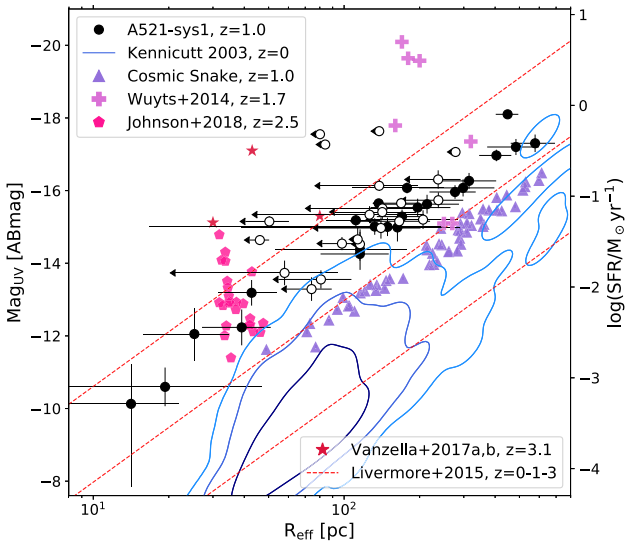

Figure 10. Intrinsic sizes and UV magnitudes of the clumps in A521-sys1 (black circles, empty markers used for size upper limits) compared to literature samples: SINGS (Kennicutt et al. 2003) at $z = 0$, shown as blue contours enclosing 68 per cent, 95 per cent, and 99.7 per cent of the sample Cosmic Snake (Cava et al. 2018) at $z = 1.0$ as purple triangles Wuyts et al. (2014), sample at $z = 1.7$ as pink plus (+) symbols Johnson et al. (2017), sample at $z = 2.5$ as fuchsia pentagons Vanzella et al. (2017a, 2017b), sources at $z = 3.1$–3.2 as red stars. Lines of median surface brightness at redshifts 0, 1, and 3 as derived by Livermore et al. (2015) are shown as red dotted lines.

Their ratio, named dynamical age $\Pi \equiv \mathrm{Age}/T_{\rm cr}$ (e.g. Gieles & Portegies Zwart 2011), is used to distinguish bound ($\Pi > 1$) and unbound ($\Pi < 1$) agglomerates (e.g. Ryon et al. 2015, 2017; Krumholz, McKee & Bland-Hawthorn 2019 for star clusters in local galaxies). Clumps in A521-sys1 have crossing times in the range $T_{\rm cr} = 0.5$–6.0 Myr. Considering the best-fitting age values we derive dynamical ages $\Pi > 1$ for most of the sample (∼90 per cent), suggesting that many clumps may be gravitationally stable against expansion. This result is discussed in light of the apparent lack of old clumps in Section 6.4. Similar fractions are found if either the SSP or the C100 models are assumed.

5.3 Extinctions

As a sanity check for the extinction values obtained, we leverage archival VLT-MUSE observations of A521 to derive extinction values in annular subregions of the galaxy, using the Balmer decrement, i.e. the observed ratio of H γ and H δ emission lines (technical details of this analysis are given in Appendix E), the depth of the VLT-MUSE data prevents us from constraining with high precision the extinction map of A521-sys1, but the analysis suggests $E(B - V)$ values below ∼0.7 mag confirming the range of extinctions found via the SED fitting process.

We perform an additional test to estimate the impact of assuming *a-priori,* an extinction value on the ages and masses derived via broad-band SED fit, this test is motivated by the lack of *HST* multiband detections affecting the study of high-z clumps (due to rest-frame optical-UV emission falling beyond the observable wavelength range), implying taking further assumptions on the clump models. We consider two models, taking the same main assumptions of the reference C10 model but limiting the range of extinction values allowed by the fit:

(i) C10-LE: the low-extinction model allowing extinctions only in the range $E(B - V) < 0.1$ mag;
(ii) C10-HE: the high-extinction model allowing extinctions only in the range $0.4 < E(B - V) < 0.5$ mag.

The results of these two models are shown in Fig. 9, as could be expected, lower (higher) extinctions force the fit to find older (younger) age values. In the case of our sample the low-extinction model is the one performing worst with the age distribution shifted by ∼0.75 dex, we point out again that masses are less affected by the choice of model and in the low-extinction model are shifted to larger values by 0.3 dex only.

6 DISCUSSION

6.1 UV size-magnitude comparison to $z = 0$–3 literature samples

We compare the intrinsic sizes and luminosities of clumps in A521-sys1, presented in Section 4.1 to other samples available in the literature in Fig. 10. Although, clump masses and ages are derived for A521-sys1 clumps, we remind that it is worth discussing UV magnitudes as tracers of the recent SFR and mass of the clumps for two main reasons: first, they are widely available for many systems both at low and high redshift (while mass estimates are much less common) and, second, they avoid comparing physical quantities typically derived using different assumptions among different samples.

In the same figure, we show the sizes and luminosities of H II regions in local ($z = 0$) main-sequence (MS) galaxies from the SINGS sample (Kennicutt et al. 2003). The SFR values of the SINGS

sample have been converted to UV magnitudes using the conversion factor in Kennicutt & Evans (2012). We observe that clumps in A521-sys1 are brighter than the ones in (Kennicutt et al. 2003) when sources at similar scales are compared, suggesting that star-forming regions in A521-sys1 are denser than local H II regions. Similar sizes and magnitudes are measured in clumps in the redshift range $z = 1$–3, we show in Fig. 10 the clumps samples of the Cosmic Snake ($z = 1.0$, Cava et al. 2018), Wuyts et al. (2014) ($z = 1.7$), Johnson et al. (2017) ($z = 2.5$), and three highly magnified clumps from Vanzella et al. (2017a), Vanzella et al. (2017b) ($z \sim 3.1$). Studies of clumps at $z \geq 1$ suggest an evolution of the clumps' average density with redshift (e.g. Livermore et al. 2015). We plot the average surface brightness at $z = 0$, 1, and 3 derived by Livermore et al. (2015), using clumps from samples of SINGS, WiggleZ (Wisnioski et al. 2012), SHiZELS (Swinbank et al. 2012), and the lensed arcs from Jones et al. (2010), Swinbank et al. (2007), Swinbank et al. (2009) and Livermore et al. (2012), our sample of clumps in A521-sys1 lies, similarly to the other samples just presented in the range of expected densities for redshifts $z = 1$–3. The main possible cause of clumps' density redshift evolution is the effect of galactic environment within galaxies (e.g Livermore et al. 2015) at higher redshift characterized by higher gas turbulence and higher hydrostatic pressure at the disc mid-plane fragmenting as denser clouds (Dessauges-Zavadsky et al. 2019; Dessauges-Zavadsky et al., in preparation). Detection limit differences could also partly explain the trends as typically galaxies at higher redshifts have worse detection limits.

Supporting the hypothesis of the (internal) galactic environmental effect studies of nearby samples of high-z analogues, e.g. GOALS LIRGs (Armus et al. 2009; Larson et al. 2020), DYNAMO gas-rich galaxies (Green et al. 2014; Fisher et al. 2017a), and LARS starbursts (Östlin et al. 2014; Messa et al. 2019) find clumps with surface densities comparable to the ones observed at redshift 1 and above. We point out that such galaxies sit above the MS for local galaxies (while instead the SINGS sample contain typical MS galaxies at $z = 0$) but are consistent with MS galaxies at $z \gtrsim 1$.

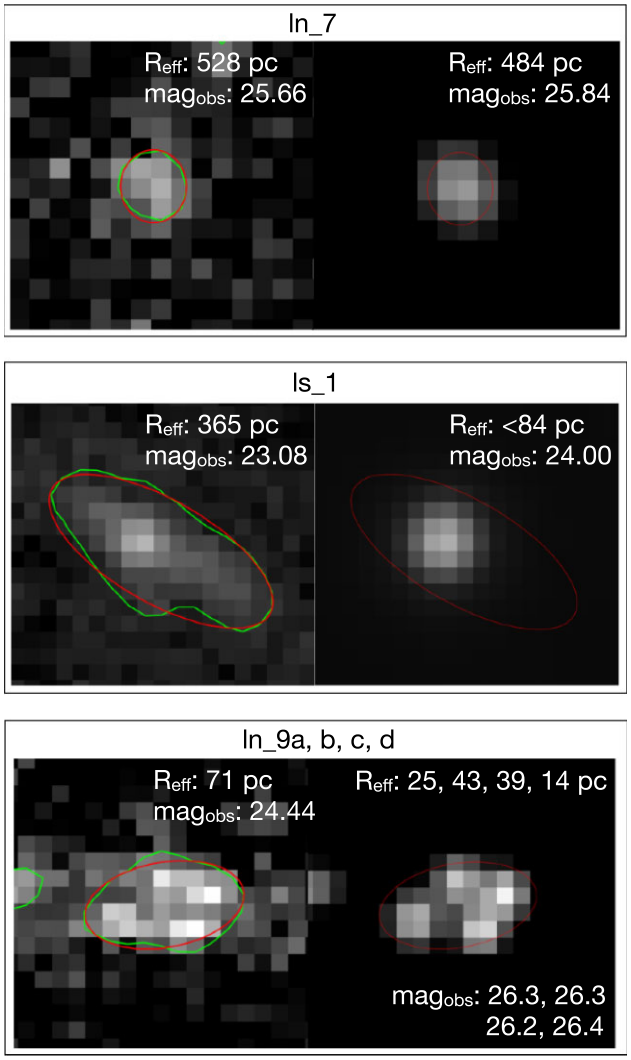

Figure 11. Examples of the extraction via 3σ contours versus the best-fitting of the 2D model. For each panel, the figure on the left shows the data with 3σ contours in green and the ellipse used for the aperture photometry and for estimating the size in red over-plotted. The figure on the right shows the best-fitting model according to the reference 2D-fit photometry. Intrinsic sizes ($R_{\rm eff}$) and observed magnitudes derived via the two methods are reported.

6.2 Properties derived via the alternative photometry method

We compare the results presented in Sections 4 and 5 to the ones obtained with the alternative extraction and photometry method introduced in Section 3.5. Overall, the alternative method miss to extract five sources (2 in CI, 1 in LN, and 2 in LS). We checked that for bright isolated sources (e.g. top panel of Fig. 11), we get similar results with the two methods (radii are different by less than a factor 1.5, magnitude differences are <0.3 mag). Large differences are observed for clumps consisting of a bright narrow peak and a diffuse tail (e.g. middle panel of Fig. 11). The 2D fit of the reference method recover only the bright peak, i.e. the densest core of the star-forming region, while the 3σ contour also include the diffuse tail. This is the case for six clumps (ci_1, ln_1, ls_1, ln_3, ln_5, and ls_5), the derived sizes can differ up to factors 4 and magnitudes up to ∼1 mag. These differences in turn convert into mass values larger by ∼1 order of magnitude and mass surface densities lower by ∼0.4 dex for sources ci_1, ln_1, and ls_1 in the case of the alternative photometry. We deduce that in the cases just mentioned,we are studying large star-forming regions via the alternative method, while the standard method focus on their dense cores.

Another class of sources where we see differences between the two methods are clumps fitted by multiple peaks in the 2D fit but falling within the same 3σ profile and therefore considered as a single source in the alternative photometry. This is the case for three clumps (the groups ln_9a, b, c, d, see bottom panel of Fig. 11, ci_7a, b, and ci_17a, b).

Despite the differences just mentioned, the overall distribution of clump sizes and $F390W$ magnitudes are similar in the two analysis, the alternative method recovers, as median values, brighter (by ∼0.5 mag) and larger (by less than a factor 1.5) clumps, but the median surface brightness of the clumps is the same with both methods. Similarly, the median mass recovered with the alternative method is larger by 0.2 dex, but its surface density is smaller (by 0.2 dex) with respect to the median values from the reference method. Age and extinction distributions are similar in the two cases. We conclude that the methodology for extracting and analysing clumps can have a strong effect especially when studying non-Gaussian or multiple-peaked systems on the other hand the average differences between considering 3σ contours or 2D Gaussian fits in our sample are negligible

6.3 Lensing effect on derived properties

Studying the same clumps imaged in the three regions introduced in Section 2.1 allows us to understand the effects of gravitational lensing on clump samples overall and on single sources. Clumps that appear similar in terms of size and magnitude on the image plane, i.e. in terms of observed properties (Fig. 3) show intrinsic properties that differ on average by a factor ∼2 in size and by ∼1 mag if clumps in CI and in LN are compared. Despite these differences, the surface brightness values observed are similar in all subregions as consequence of its conservation through gravitational lensing. The mass values resulting from the SED fitting confirm the photometric results as clumps in the CI region appear more massive by 0.5 dex compared to the ones in LN, but median surface densities are similar in all subregions. Overall, we are able to observe on an average smaller less-massive clumps in regions with larger magnification, but the distribution of such properties are not drastically different in the three subregions. The clumpiness estimates are also similar (Fig. 5) and the slightly lower values retrieved in LN can be mainly attributed by the presence of a bright foreground galaxy, difficult to subtract completely from the data (Section 4.2).

Moving from the overall distributions to one-to-one analysis of individual clumps as observed in CI, LN, and LS, we find that clumps with magnification differences smaller than a factor ∼2 between one image and another, e.g. source 4 (ci_4, ln_4, and ls_4 have $\mu = 4.8$, 3.4, and 3.4 respectively) display similar photometric and physical properties, consistent within uncertainties. On the other hand, larger differences can be observed when clumps are greatly magnified in some subregions, as for clump 1 with an amplification $\mu = 11$ in the LN image (ln_1) but $\mu = 3.7$ in the CI (ci_1) in the latter case the derived mass value is larger by 0.25 dex but with a lower limit on the mass density which is 0.25 dex smaller than the one derived for ln_1. A similar case is clump 9 (bottom right-hand panel of Fig. 11), which in the LS region (magnification $\mu = 5$) appears like a single-peaked source with an estimated size upper limit $R_{\rm eff} < 200$ pc, but with the large magnification of the LN region ($\mu \gtrsim 50$) can be separated into four narrow peaks with physical scales between 15 and 50 pc. Individual subpeaks have smaller derived sizes and masses than the single source ls_9, but their derived mass surface densities are larger, suggesting that at smaller physical scales we are able to observe denser cores of clumps (Fig. 8), such trend is confirmed by simulations of resolution effects on derived clump properties (Meng & Gnedin 2020).

One extreme case is clump 8 being magnified by $\mu = 20$ in the LN and LS images, compared to $\mu = 3.5$ in the CI in case of ci_8, we derive a mass of $\log(M/{\rm M}_\odot) = 8.3$, more than one order of magnitude larger than for ln_8 and ls_8 ($\log(M/{\rm M}_\odot) = 7.0$ and 7.1), also its mass surface density is one order of magnitude larger than what is found for ln_8 and ls_8. We attribute such large values of mass and density to the position of ci_8 being consistent with the bulge of the galaxy and with a massive cloud of molecular gas, as found by the analysis of Dessauges-Zavadsky et al. (in preparation). Its derived age 20 Myr seems to suggest that some star formation is still going on even there. The image of clump 8 on the lensed arc is heavily distorted and magnified, therefore what we observe as ln_8 and ls_8 could be a dense star-forming core within source 8 itself.

6.4 Galactocentric trends

Focusing on the CI, where the entire galaxy can be studied with an almost uniform magnification, we test for possible radial trends of A521-sys1 clumps' properties. In Fig. 12, we plot the positions of clumps in the CI, colour-coded by their derived properties, on the *F*814*W* observations. Radial trends in clumps' ages and masses can be used to test their survival and evolution within the host galaxies and, as a consequence to test formation models of galaxies and their bulges. The presence of older and more massive clumps near the centre of the galaxy has been interpreted as a sign of the more massive clumps being able to survive bound for hundred of Myr, migrating toward the centre of the galaxy and there merging to form the galactic bulge, as suggested by simulations by e.g. Bournaud et al. 2007; Krumholz & Dekel 2010, while other simulations argue that such migrating clumps would have marginal effect on bulge growth (e.g. Tamburello et al. 2015). Running Spearman's correlation test we do not find any statistically significant correlation between the clump physical properties plotted in Fig. 12 and the galactocentric radius. We observe massive clumps all over the spiral arms with the most massive one being at ∼7.5 kpc from the centre (ci_14). In the same way, we observe dense clumps both very close to the centre and further away along the spiral arms (e.g. ci_4). In particular, we observe two massive clumps close to the centre of the galaxy, namely ci_1 and ci_8 (the latter sitting at the coordinates of the bulge, Nagy et al. 2021), their young ages (4 and 20 Myr, respectively) suggest that star formation is taking place also at the centre of the galaxy. At the same time, the large mass, $\log(M/{\rm M}_\odot) = 8.3$, and density, $\langle\Sigma_M\rangle > 10^3\ {\rm M}_\odot\ {\rm pc}^{-2}$ of clump ci_8 may suggest that we are looking at the formation of a proto-bulge.

Fig. 12 suggests the presence of an age and extinction asymmetry between the two spiral arms with the western arm being younger and more extincted than the eastern one. The difference is small (on average ∼20 Myr in age and 0.1 mag in colour excess) but consistent across the stellar models tested. Asymmetries are very common in late-type galaxies but the uncertainties associated to the derived ages prevent us to drive robust conclusions for A521-sys1.

Another useful metric to test the possible migration of clumps is the dynamic time of the galaxy, defined as the ratio between the rotation velocity and the radius, when compared to the age of the clumps it probes whether a clump is still close to the natal region, age $\lesssim {\rm t}_{\rm dyn}$, or it had survived enough $t_{\rm dyn}$ to have possibly migrated age $\gtrsim 10 \times t_{\rm dyn}$ (e.g. Förster Schreiber et al. 2011b; Adamo et al. 2013). Considering the rotation curve of A521-sys1 (Patrício et al. 2018, from MUSE data), we derive a $t_{\rm dyn}$ varying from ∼10 Myr near the centre to ∼100 Myr at 6 kpc, these values are consistent with the ages spanned by the clumps, indicating that they observed close to their natal region. In addition, the clumpiness analysis (Section 4.2) show that clumps are not dominating the light at wavelengths longer than (rest-frame) ≳3000 Å, suggesting that clumps are not surviving as bound structures for time-scales longer than 100 Myr.

The lack of old and migrating clumps seems in contrast with the large dynamical ages retrieved (Section 5.2), suggesting that clumps should be gravitationally stable against expansions. One possible cause of this inconsistency could be that the dynamical age is not a suitable metric for the gravitational stability of clumps at scales >10 pc, dynamical ages were introduced to study the stability of stellar clusters on scales of few pc and assuming virial equilibrium (Gieles & Portegies Zwart 2011). On the other hand, stellar evolution changes the clump colours to redder values such that a 500 Myr old clump with $M = 2 \cdot 10^7\ {\rm M}_\odot$ (the median value for our sample, found in Section 5) would have at the distance of A521-sys1 an observed magnitude of 29.64 mag in *F*814*W* (and fainter magnitudes in bluer filters), while the depth of the observations in *F*814*W* reaches 27.5 mag (Table 1), the completeness within A521-sys is shallower by >0.5 mag, and therefore we would expect to observe such old clumps only in case of large magnifications, $\mu \gtrsim 10$, thus only in

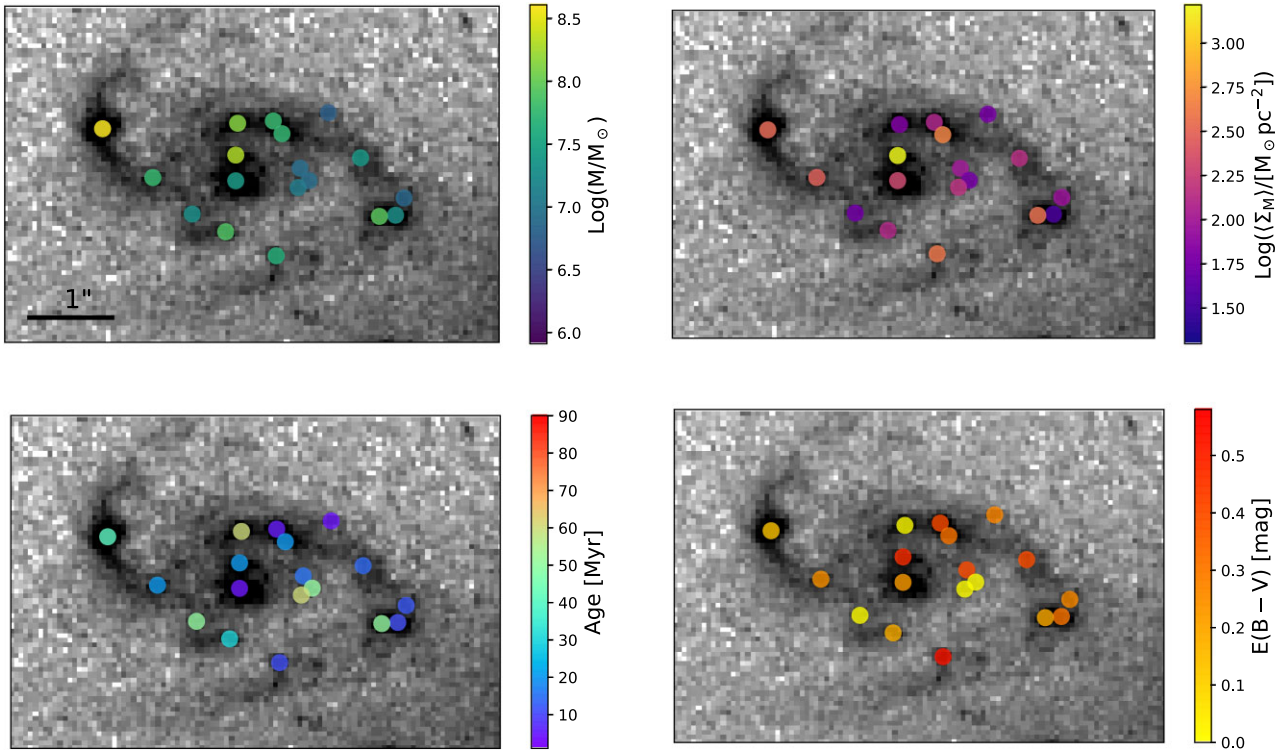

Figure 12. F814W observations of the CI region with the position of detected clumps, colour-coded by their derived mass (top-left), mass surface density (top-right), age (bottom-left), and extinction (bottom-right). The Spearman's correlation test do not recover significant any correlations between the galactocentric distance of the clumps and their properties shown here.

limited regions. Moving to the NIR filters (*F*105*W* and *F*160*W*) would result in brighter observed magnitudes, but, at the cost of worse spatial resolution and worse completeness, leading similarly to low chances of observing old clumps in A521-sys1.

7 CONCLUSIONS

We analysed the clump population of the gravitationally-lensed galaxy A521-sys1, a $z = 1.04$ galaxy with properties typical of main sequence systems at similar redshift, i.e. elevated star formation (SFR $= 16 \pm 5\,M_\odot yr^{-1}$) and gas-rich rotation-dominated disc with high-velocity dispersion (Patrício et al. 2018; Girard et al. 2019; Nagy et al. 2021). A521-sys1 is characterized by a clumpy morphology in the NUV band observed with *HST WFC*3-*F*390*W*, we use this as the reference filter for extracting the clump catalogue and study the sizes and rest-frame UV photometry. Four additional *HST* filters, *F*606*W*, *F*814*W* from ACS and *F*105*W*, *F*160*W* from *WFC*3/IR, are used to characterize ages and masses of the clumps via broad-band SED fitting.

The appearance of A521-sys is heavily affected by gravitational lensing, producing multiple images of the same system and allowing the study of clumps seen at different intrinsic scales in the range 10–600 pc. Roughly half of the galaxy is stretched into a wide arc with magnification μ, reaching factors 10 and above, the arc is made by two mirrored images, which we call lensed-north (LN) and lensed-south (LS). The entire system is observable via a counter-image (CI) with a mean magnification $\mu \sim 4$. A gravitational lens model is constructed for the entire A521 galaxy cluster (Richard et al. 2010) and is later fine-tuned to constrain with better precision the area enclosing the A521-sys1 images, giving a final positional accuracy of 0.08 arcsec, comparable to the pixel scale of the *HST* observations.

We derive the following results via photometric and broad-band SED analyses:

(i) we extract a sample of 18 unique clumps, many of those are imaged multiple times and some are resolved into subclumps when observed at high magnifications. As a consequence, the final sample counts 45 entries;

(ii) the intrinsic clump sizes range from ∼10 to ∼600 pc, suggesting that we are observing systems that span from almost single clusters to large star-forming regions. Scales below ∼50 pc are resolved only in the LN region, hosting small areas close to the critical lines with extreme magnifications ($\mu > 20$). Half of the recovered values are upper limits, suggesting that in many cases clumps are more compact that what we are able to resolve;

(iii) the interval of absolute UV clump magnitudes is comparable to the ones of other literature clump samples at similar redshift and at similar physical scales. We confirm that the surface brightnesses of clumps in $z \gtrsim 1$ galaxies are much larger than the corresponding star-forming regions in local galaxies. On the other hand, the complete analysis reveals that, given the depth of our observations, we would not be able to observe clumps with lower surface brightness;

(iv) the galaxy appears less clumpy in redder bands, this is quantitatively confirmed by the clumpiness analysis, measuring what fraction of the galaxy luminosity is produced by clumps. The clumpiness is high (around 40 per cent) in rest-frame NUV, suggesting that a large fraction of the recent star formation is taking place in the clumps we observe, and decreases moving to *V* and *I*

bands, where the old stellar population of the galaxy dominates the emission;

(v) the derived clump masses range from $10^{5.9}$ to $10^{8.6}\,M_\odot$, confirming that we are studying both cluster or cluster aggregations and large star-forming regions. The overall mass distribution and its median value ($\sim 2 \cdot 10^7\,M_\odot$) do not change considerably if either a 10 Myr continuum star formation models (C10, used as reference), a single stellar population model (SSP) or a 100 Myr continuum star formation model are considered, the same is true when testing different extinction models (Cardelli et al. 1989 and Calzetti et al. 2000) and different metallicities.
The clump sample has a median mass surface density of $\sim 10^2\,M_\odot\,pc^{-2}$ but few clumps reach densities typical of the most massive compact (<5 pc) stellar clusters observed in local galaxies ($\sim 10^3\,M_\odot\,pc^{-2}$). No statistically significant galactocentric trend is observed with either mass or mass density. Dense and massive clumps are observed both close to the galactic bulge and along the outskirts of the spiral arms;

(vi) the majority of derived ages are <100 Myr with many clumps having a best-fit age close to 10 Myr. Clumps of such young ages are consistent with being observed close to their natal region, making impossible to the study of possible clump migration. The study of the dynamical age defined by the comparison between clump ages and their density suggests that most of the clumps may be gravitationally stable against expansion;

(vii) clump extinctions are distributed in the range $E(B-V) =$ 0.0–0.6 mag, consistent with the analysis of the Balmer decrement derived from VLT-MUSE observations. Testing the SED fitting with extinction fixed in narrow intervals reveals that inaccurate assumptions (e.g. $E(B-V) \sim 0.0$ mag for the entire sample) would result in biasing the derived ages by roughly a factor 10, while having a much smaller impact on the masses;

(viii) the lack of galactocentric trends for any of the physical properties available and the lack of old migrated clumps can be explained either by dissolution of clumps after few ∼100 Myr or by stellar evolution making them fall below the detectability limits of our data.

(ix) when comparing the properties observed in different galaxy images (CI, LN, and LS), clumps appear on average smaller and less bright (and less massive) in LN, suggesting that in regions with large magnifications, we are able to observe the cores of the >100 pc star-forming regions seen with no or little magnification. Surface brightnesses and mass surface densities are overall very similar in all sub-regions.

ACKNOWLEDGEMENTS

We thank the anonymous referee for the useful comments that helped improving the quality of the paper. This research made use of Photutils, an Astropy package for detection and photometry of astronomical sources (Bradley et al. 2020). M.M. acknowledges the support of the Swedish Research Council, Vetenskapsrådet (internationell postdok grant 2019-00502).

DATA AVAILABILITY

The *HST* data underlying this article are accessible from the Hubble Legacy Archive (HLA) at https://hla.stsci.edu/ or through the MAST portal at https://mast.stsci.edu/portal/Mashup/Clients/Mast/Portal.html (proposal IDs 15435 and 16670). The derived data generated in this research will be shared on reasonable request to the corresponding author.

REFERENCES

Adamo A., Östlin G., Bastian N., Zackrisson E., Livermore R. C., Guaita L., 2013, ApJ, 766, 105
Armus L. et al., 2009, PASP, 121, 559
Bastian N., Lardo C., 2018, ARA&A, 56, 83
Bertin E., Arnouts S., 1996, A&AS, 117, 393
Bik A., Östlin G., Hayes M., Adamo A., Melinder J., Amram P., 2015, A&A, 576, L13
Bik A., Östlin G., Menacho V., Adamo A., Hayes M., Herenz E. C., Melinder J., 2018, A&A, 619, A131
Bournaud F., Elmegreen B. G., Elmegreen D. M., 2007, ApJ, 670, 237
Bournaud F., Elmegreen B. G., Martig M., 2009, ApJ, 707, L1
Bournaud F., Dekel A., Teyssier R., Cacciato M., Daddi E., Juneau S., Shankar F., 2011, ApJ, 741, L33
Bournaud F. et al., 2014, ApJ, 780, 57
Bournaud F., Daddi E., Weiß A., Renaud F., Mastropietro C., Teyssier R., 2015, A&A, 575, A56
Bouwens R. J., Illingworth G. D., Oesch P. A., Caruana J., Holwerda B., Smit R., Wilkins S., 2015, ApJ, 811, 140
Bradley L. et al., 2020, astropy/photutils: 1.0.0. Zenodo, available at https://doi.org/10.5281/zenodo.4044744
Brinchmann J., Charlot S., White S. D. M., Tremonti C., Kauffmann G., Heckman T., Brinkmann J., 2004, MNRAS, 351, 1151
Brown G., Gnedin O. Y., 2021, MNRAS, 508, 5935
Calzetti D., Armus L., Bohlin R. C., Kinney A. L., Koornneef J., Storchi-Bergmann T., 2000, ApJ, 533, 682
Cappellari M., 2017, MNRAS, 466, 798
Cardelli J. A., Clayton G. C., Mathis J. S., 1989, ApJ, 345, 245
Carollo C. M., Scarlata C., Stiavelli M., Wyse R. F. G., Mayer L., 2007, ApJ, 658, 960
Cava A., Schaerer D., Richard J., Pérez-González P. G., Dessauges-Zavadsky M., Mayer L., Tamburello V., 2018, Nat. Astron., 2, 76
Cowie L. L., Hu E. M., Songaila A., 1995, AJ, 110, 1576
Daddi E. et al., 2010, ApJ, 713, 686
Dekel A., Sari R., Ceverino D., 2009, ApJ, 703, 785
Dessauges-Zavadsky M. et al., 2019, Nat. Astron., 3, 1115
Dessauges-Zavadsky M., Richard J., Combes F.,Messa M., Nagy D.,Mayer L.,Schaerer D., Egami E., 2022, MNRAS, submitted
Dopita M. A., Sutherland R. S., 2003, Astrophysics of the Diffuse Universe. Springer, Berlin, New York
Elmegreen B. G., Elmegreen D. M., 2005, ApJ, 627, 632
Elmegreen D. M., Elmegreen B. G., Rubin D. S., Schaffer M. A., 2005, ApJ, 631, 85
Elmegreen D. M., Elmegreen B. G., Ravindranath S., Coe D. A., 2007, ApJ, 658, 763
Elmegreen B. G., Bournaud F., Elmegreen D. M., 2008, ApJ, 688, 67
Elmegreen B. G., Elmegreen D. M., Fernandez M. X., Lemonias J. J., 2009, ApJ, 692, 12
Ferland G. J. et al., 2013, RMxAA, 49, 137
Fisher D. B. et al., 2017a, MNRAS, 464, 491
Fisher D. B. et al., 2017b, ApJ, 839, L5
Förster Schreiber N. M. et al., 2006, ApJ, 645, 1062
Förster Schreiber N. M., Shapley A. E., Erb D. K., Genzel R., Steidel C. C., Bouché N., Cresci G., Davies R., 2011a, ApJ, 731, 65
Förster Schreiber N. M. et al., 2011b, ApJ, 739, 45
Gabor J. M., Bournaud F., 2013, MNRAS, 434, 606
Gaia Collaboration, 2018, A&A, 616, A1
Genzel R. et al., 2006, Nature, 442, 786
Genzel R. et al., 2008, ApJ, 687, 59
Genzel R. et al., 2015, ApJ, 800, 20
Gieles M., Portegies Zwart S. F., 2011, MNRAS, 410, L6
Girard M., Dessauges-Zavadsky M., Combes F., Chisholm J., Patrício V., Richard J., Schaerer D., 2019, A&A, 631, A91
Goldbaum N. J., Krumholz M. R., Forbes J. C., 2016, ApJ, 827, 28
Green A. W. et al., 2014, MNRAS, 437, 1070
Guo Y., Giavalisco M., Ferguson H. C., Cassata P., Koekemoer A. M., 2012, ApJ, 757, 120

Herenz E. C., Hayes M., Papaderos P., Cannon J. M., Bik A., Melinder J., Östlin G., 2017, A&A, 606, L11
Hoffmann S. L., Mack J., Avila R., Martlin C., Cohen Y., Bajaj V., 2021, BAAS, 53, 216.02
Hopkins P. F., Quataert E., Murray N., 2012, MNRAS, 421, 3488
Immeli A., Samland M., Gerhard O., Westera P., 2004a, A&A, 413, 547
Immeli A., Samland M., Westera P., Gerhard O., 2004b, ApJ, 611, 20
Jedrzejewski R. I., 1987, MNRAS, 226, 747
Johnson T. L. et al., 2017, ApJ, 843, L21
Jones T. A., Swinbank A. M., Ellis R. S., Richard J., Stark D. P., 2010, MNRAS, 404, 1247
Jullo E., Kneib J. P., Limousin M., Elíasdóttir Á., Marshall P. J., Verdugo T., 2007, New J. Phys., 9, 447
Kennicutt R. C., Evans N. J., 2012, ARA&A, 50, 531
Kennicutt Robert C. J. et al., 2003, PASP, 115, 928
Kewley L. J., Dopita M. A., 2002, ApJS, 142, 35
Kroupa P., 2001, MNRAS, 322, 231
Krumholz M. R., Dekel A., 2010, MNRAS, 406, 112
Krumholz M. R., McKee C. F., Bland -Hawthorn J., 2019, ARA&A, 57, 227
Larson K. L. et al., 2020, ApJ, 888, 92
Leitherer C. et al., 1999, ApJS, 123, 3
Livermore R. C. et al., 2012, MNRAS, 427, 688
Livermore R. C. et al., 2015, MNRAS, 450, 1812
Ma X. et al., 2018, MNRAS, 477, 219
Mandelker N., Dekel A., Ceverino D., Tweed D., Moody C. E., Primack J., 2014, MNRAS, 443, 3675
Mandelker N., Dekel A., Ceverino D., DeGraf C., Guo Y., Primack J., 2017, MNRAS, 464, 635
Meng X., Gnedin O. Y., 2020, MNRAS, 494, 1263
Messa M., Adamo A., Östlin G., Melinder J., Hayes M., Bridge J. S., Cannon J., 2019, MNRAS, 487, 4238
Meštrić U. et al., 2022, preprint (arXiv:2202.09377)
Mieda E., Wright S. A., Larkin J. E., Armus L., Juneau S., Salim S., Murray N., 2016, ApJ, 831, 78
Nagy D., Dessauges-Zavadsky M., Richard J., Schaerer D., Combes F., Messa M., Chisholm J., 2021, A&A, 657, A25
Newville M. et al., 2021, lmfit/lmfit-py 1.0.2. Zenodo, availabale at https://doi.org/10.5281/zenodo.4516651
Noguchi M., 1999, ApJ, 514, 77
Oklopčić A., Hopkins P. F., Feldmann R., Kereš D., Faucher-Giguère C.-A., Murray N., 2017, MNRAS, 465, 952
Östlin G. et al., 2014, ApJ, 797, 11
Patrício V. et al., 2018, MNRAS, 477, 18
Planck Collaboration, 2014, A&A, 571, A16
Renaud F., Romeo A. B., Agertz O., 2021, MNRAS, 508, 352
Richard J. et al., 2010, MNRAS, 404, 325
Richard J. et al., 2014, MNRAS, 444, 268
Rivera-Thorsen T. E. et al., 2019, Science, 366, 738
Ryon J. E. et al., 2015, MNRAS, 452, 525
Ryon J. E. et al., 2017, ApJ, 841, 92
Salpeter E. E., 1955, ApJ, 121, 161
Shapiro K. L. et al., 2008, ApJ, 682, 231
Soto E. et al., 2017, ApJ, 837, 6
Speagle J. S., Steinhardt C. L., Capak P. L., Silverman J. D., 2014, ApJS, 214, 15
Storey P. J., Hummer D. G., 1995, MNRAS, 272, 41
Swinbank A. M., Bower R. G., Smith G. P., Wilman R. J., Smail I., Ellis R. S., Morris S. L., Kneib J. P., 2007, MNRAS, 376, 479
Swinbank A. M. et al., 2009, MNRAS, 400, 1121
Swinbank A. M., Smail I., Sobral D., Theuns T., Best P. N., Geach J. E., 2012, ApJ, 760, 130
Tacconi L. J. et al., 2010, Nature, 463, 781
Tacconi L. J. et al., 2013, ApJ, 768, 74
Tamburello V., Mayer L., Shen S., Wadsley J., 2015, MNRAS, 453, 2490
Tamburello V., Rahmati A., Mayer L., Cava A., Dessauges-Zavadsky M., Schaerer D., 2017, MNRAS, 468, 4792
Tremonti C. A. et al., 2004, ApJ, 613, 898
van den Bergh S., Abraham R. G., Ellis R. S., Tanvir N. R., Santiago B. X., Glazebrook K. G., 1996, AJ, 112, 359
van Donkelaar F., Agertz O., Renaud F., 2021, MNRAS, 512, 3806
Vanzella E. et al., 2017a, MNRAS, 467, 4304
Vanzella E. et al., 2017b, ApJ, 842, 47
Vanzella E. et al., 2019, MNRAS, 483, 3618
Vanzella E. et al., 2021a, A&A, 646, A57
Vanzella E. et al., 2021b, A&A, 659, A2
Vázquez G. A., Leitherer C., 2005, ApJ, 621, 695
Wisnioski E., Glazebrook K., Blake C., Poole G. B., Green A. W., Wyder T., Martin C., 2012, MNRAS, 422, 3339
Wisnioski E. et al., 2018, ApJ, 855, 97
Wuyts E., Rigby J. R., Gladders M. D., Sharon K., 2014, ApJ, 781, 61
Zackrisson E., Rydberg C.-E., Schaerer D., Östlin G., Tuli M., 2011, ApJ, 740, 13
Zanella A. et al., 2015, Nature, 521, 54
Zanella A. et al., 2019, MNRAS, 489, 2792

APPENDIX A: SUPPLEMENTARY PHOTOMETRIC TABLE AND FIGURES

We report in Table A1, the clump photometry in all filters, we provide apparent magnitudes (and uncertainties), corrected for Galactic reddening, but uncorrected for lensing. Data, best-fitting clump models and fit residuals in *F*390*W* are shown in Fig. A1, the observations in all the the other filters are shown in Fig. A2.

Table A1. Apparent AB magnitudes (and relative uncertainties), corrected for Galactic reddening. Empty entries indicate a non-detection in the corresponding filter.

ID (0)	mag$_{F390W}$ (1)	mag$_{F606W}$ (2)	mag$_{F814W}$ (3)	mag$_{F105W}$ (4)	mag$_{F160W}$ (5)
ci_1	$24.45^{\pm0.05}$	$24.34^{\pm0.05}$	$24.30^{\pm0.10}$	$24.12^{\pm0.21}$	$24.71^{\pm0.05}$
ci_3	$25.75^{\pm0.21}$	$25.56^{\pm0.09}$	$24.89^{\pm0.11}$	$24.74^{\pm0.07}$	$24.42^{\pm0.07}$
ci_4	$26.79^{\pm0.21}$	$25.72^{\pm0.08}$	$25.17^{\pm0.08}$	$24.67^{\pm0.07}$	$24.22^{\pm0.07}$
ci_5	$26.39^{\pm0.21}$	$26.69^{\pm0.21}$	$26.02^{\pm0.21}$	$26.04^{\pm0.26}$	$26.64^{\pm0.64}$
ci_7a	$26.02^{\pm0.23}$	$25.39^{\pm0.14}$	$24.82^{\pm0.12}$	$24.36^{\pm0.08}$	$24.26^{\pm0.10}$
ci_7b	$25.43^{\pm0.22}$	$25.10^{\pm0.13}$	$24.74^{\pm0.16}$	$24.50^{\pm0.09}$	$24.36^{\pm0.11}$
ci_8	$26.01^{\pm0.13}$	$25.89^{\pm0.11}$	$25.25^{\pm0.10}$	$24.23^{\pm0.07}$	$23.33^{\pm0.07}$
ci_9a	$27.44^{\pm0.33}$	$27.63^{\pm0.05}$	$27.84^{\pm0.05}$	$26.42^{\pm0.05}$	$26.00^{\pm0.05}$
ci_9b	$26.91^{\pm0.24}$	$27.30^{\pm0.05}$	$26.98^{\pm0.05}$	$26.63^{\pm0.05}$	–
ci_9c	$27.26^{\pm0.32}$	$27.28^{\pm0.05}$	$26.33^{\pm0.05}$	$26.05^{\pm0.05}$	$26.88^{\pm0.05}$
ci_10	$26.83^{\pm0.38}$	$26.37^{\pm0.18}$	$25.81^{\pm0.18}$	$25.15^{\pm0.15}$	$24.76^{\pm0.12}$
ci_11	$26.38^{\pm0.15}$	$25.96^{\pm0.12}$	$25.82^{\pm0.19}$	$25.60^{\pm0.05}$	$25.36^{\pm0.25}$
ci_14	$24.30^{\pm0.10}$	$24.06^{\pm0.07}$	$23.58^{\pm0.08}$	$23.30^{\pm0.07}$	$23.09^{\pm0.08}$
ci_15a	$25.06^{\pm0.05}$	$24.66^{\pm0.08}$	$24.32^{\pm0.11}$	$23.91^{\pm0.05}$	$24.21^{\pm0.05}$
ci_15b	$26.43^{\pm0.05}$	$26.13^{\pm0.16}$	$25.46^{\pm0.13}$	$25.26^{\pm0.05}$	$24.40^{\pm0.05}$
ci_16	$24.88^{\pm0.23}$	$24.64^{\pm0.09}$	$24.07^{\pm0.14}$	$23.93^{\pm0.08}$	$24.29^{\pm0.19}$
ci_17	$26.68^{\pm0.23}$	$25.96^{\pm0.09}$	$26.18^{\pm0.13}$	$25.93^{\pm0.11}$	$26.63^{\pm0.36}$
ci_18	$26.18^{\pm0.14}$	$25.49^{\pm0.08}$	$25.29^{\pm0.10}$	$24.98^{\pm0.11}$	$24.52^{\pm0.12}$
ln_1	$23.34^{\pm0.05}$	$23.14^{\pm0.05}$	$23.32^{\pm0.06}$	$23.78^{\pm0.05}$	$23.51^{\pm0.08}$
ln_2	$25.00^{\pm0.12}$	$24.51^{\pm0.06}$	$24.68^{\pm0.07}$	$24.58^{\pm0.07}$	$24.47^{\pm0.05}$
ln_3	$25.86^{\pm0.23}$	$25.23^{\pm0.10}$	$24.68^{\pm0.09}$	$24.36^{\pm0.08}$	$24.22^{\pm0.08}$
ln_4	$27.19^{\pm0.27}$	$26.18^{\pm0.11}$	$25.66^{\pm0.11}$	$25.09^{\pm0.09}$	$24.73^{\pm0.08}$
ln_5	$25.95^{\pm0.17}$	$25.90^{\pm0.13}$	$25.68^{\pm0.19}$	$25.37^{\pm0.11}$	$25.39^{\pm0.10}$
ln_6	$26.72^{\pm0.33}$	$26.01^{\pm0.15}$	$25.86^{\pm0.17}$	$25.47^{\pm0.18}$	$26.08^{\pm0.26}$
ln_7	$25.84^{\pm0.16}$	$25.41^{\pm0.10}$	$24.81^{\pm0.10}$	$24.62^{\pm0.11}$	$24.74^{\pm0.18}$
ln_8	$25.71^{\pm0.16}$	$25.20^{\pm0.08}$	$24.77^{\pm0.11}$	$24.35^{\pm0.08}$	$23.88^{\pm0.05}$
ln_9	$26.13^{\pm0.15}$	$25.95^{\pm0.13}$	$25.34^{\pm0.13}$	$25.07^{\pm0.12}$	$25.52^{\pm0.41}$
ln_9a	$26.25^{\pm0.18}$	$25.98^{\pm0.05}$	$25.53^{\pm0.18}$	$25.17^{\pm0.05}$	$25.19^{\pm0.05}$
ln_9b	$26.29^{\pm0.18}$	$25.63^{\pm0.05}$	$25.21^{\pm0.14}$	$24.94^{\pm0.05}$	$24.84^{\pm0.05}$
ln_9c	$26.19^{\pm0.19}$	$25.53^{\pm0.05}$	$24.77^{\pm0.10}$	$24.27^{\pm0.05}$	$24.06^{\pm0.05}$
ln_9d	$26.35^{\pm0.20}$	$26.07^{\pm0.05}$	$25.75^{\pm0.23}$	$25.67^{\pm0.05}$	$26.73^{\pm0.05}$
ln_10	$26.10^{\pm0.13}$	$25.79^{\pm0.10}$	$25.31^{\pm0.14}$	$25.29^{\pm0.19}$	$25.98^{\pm0.85}$
ln_12	$25.96^{\pm0.21}$	$25.43^{\pm0.09}$	$25.18^{\pm0.05}$	$25.33^{\pm0.09}$	–
ln_13	$27.02^{\pm0.37}$	$28.44^{\pm0.72}$	$28.77^{\pm0.05}$	–	–
ls_1	$24.00^{\pm0.05}$	$23.81^{\pm0.06}$	$23.93^{\pm0.07}$	$23.91^{\pm0.05}$	$24.31^{\pm0.11}$
ls_2	$25.33^{\pm0.08}$	$24.74^{\pm0.07}$	$24.51^{\pm0.07}$	$24.75^{\pm0.07}$	$24.73^{\pm0.05}$
ls_3	$26.42^{\pm0.19}$	$25.67^{\pm0.07}$	$25.46^{\pm0.09}$	$24.94^{\pm0.08}$	$24.68^{\pm0.05}$
ls_4	$27.00^{\pm0.23}$	$26.00^{\pm0.08}$	$25.29^{\pm0.09}$	$24.87^{\pm0.07}$	$24.50^{\pm0.07}$
ls_5	$26.25^{\pm0.18}$	$26.17^{\pm0.12}$	$26.02^{\pm0.18}$	$25.62^{\pm0.18}$	$25.67^{\pm0.22}$
ls_6	$25.67^{\pm0.17}$	$25.39^{\pm0.11}$	$24.89^{\pm0.12}$	$24.72^{\pm0.11}$	$24.56^{\pm0.05}$
ls_7	$25.20^{\pm0.15}$	$24.88^{\pm0.08}$	$24.22^{\pm0.09}$	$23.96^{\pm0.08}$	$23.85^{\pm0.09}$
ls_8	$26.10^{\pm0.15}$	$25.15^{\pm0.08}$	$24.86^{\pm0.10}$	$24.32^{\pm0.09}$	$23.92^{\pm0.09}$
ls_9	$26.55^{\pm0.25}$	$26.03^{\pm0.11}$	$25.90^{\pm0.13}$	$25.36^{\pm0.11}$	$25.75^{\pm0.05}$
ls_11	$26.46^{\pm0.13}$	$26.03^{\pm0.09}$	$25.98^{\pm0.16}$	$25.30^{\pm0.09}$	$25.20^{\pm0.05}$
ls_12	$26.57^{\pm0.22}$	$26.17^{\pm0.16}$	$26.11^{\pm0.25}$	$26.37^{\pm0.26}$	$27.33^{\pm0.88}$

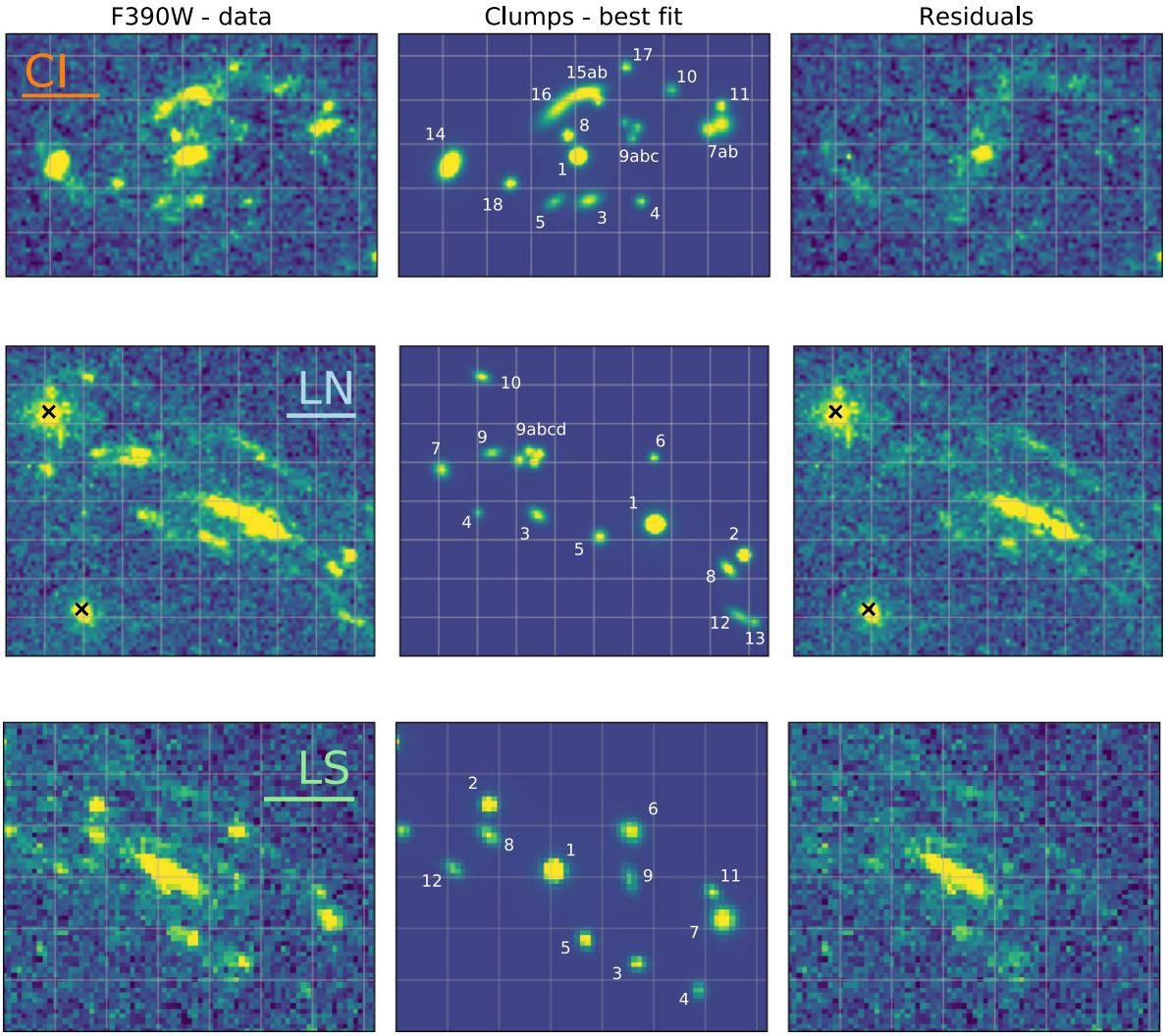

Figure A1. *F390W* observations (left-hand column), best-fitting *F390W* models (central column), and residuals (right-hand column) for the three A521-sys1 subregions CI (top row), LN (middle row), and LS (bottom row). In each case a line corresponding to 1 arcsec is given at the bottom of the subregion name. Foreground galaxies are marked as black crosses in the LN panels. Clumps IDs are reported in the central panels. The bright residual in the inner part of the galaxy corresponds to the 'tail' of clump 1, while it is not considered as a source in the reference photometry, it is analysed when the alternative photometric method is adopted, as discussed in Section 6.2 of the main text. Grids with 0.6 arcsec size are plotted to facilitate the comparison between panels.

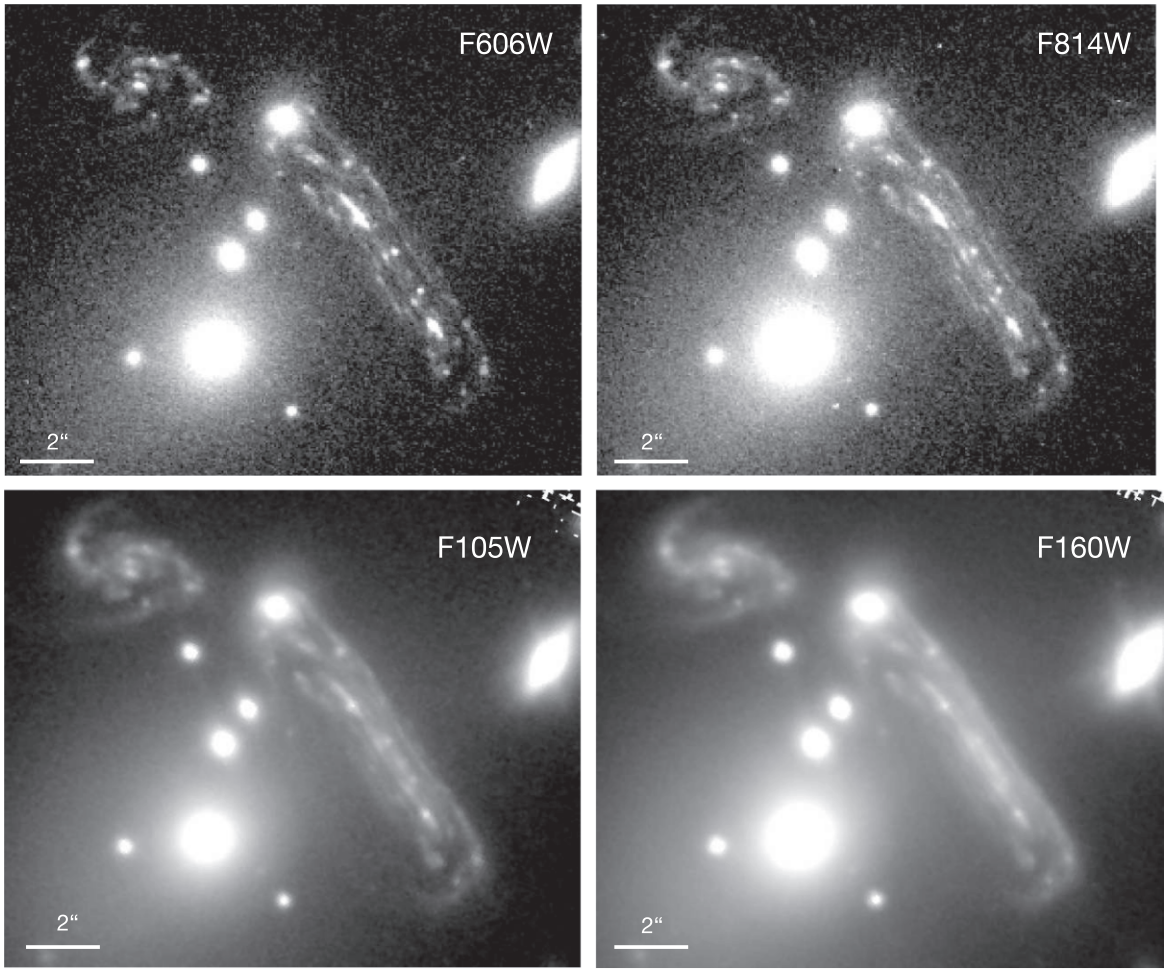

Figure A2. Observations for *F*606*W*, *F*814*W*, *F*105*W*, and *F*160*W*, corresponding to rest-frame central wavelengths of 2900, 3900, 5200, and 7500 Å. The complete photometry of the clump sample is presented in Table A1. As discussed in Section 4.2 of the main text, the galaxy appears less clumpy when moving to longer wavelengths.

APPENDIX B: UPDATE ON LENSING MODEL

The starting point of our lens model is the LoCuSS cluster mass model presented in Richard et al. (2010), which was based on a limited number of star-forming clumps in the giant arc at $z = 1$. The cluster RXCJ0454 has the smallest Einstein radius (3.6 arcsec) among the 20 LoCuSS clusters analysed in Richard et al. (2010), making it more similar to a group-like lens dominated by the brightest cluster galaxy (BCG). We have followed here the same approach in the parametrization but improved the model to include new constraints from *HST* images and cluster members identified in the MUSE observations, and summarize here the elements of the modelling. The mass distribution of the cluster is parametrized as the sum of double Pseudo Isothermal Elliptical (dPIE) potentials: 1 cluster-scale component and multiple galaxy-scale components. These potentials are characterized by the centre ellipticity and position angle velocity dispersion σ and two characteristic radii $r_{\rm core}$ and $r_{\rm cut}$.

We have selected colour-selected cluster members from Richard et al. (2010), complemented by spectroscopically-confirmed cluster members from MUSE, leading to a total of 52 galaxy-scale cluster members (indicated with white arrows in Fig. B1). To reduce the number of free parameters in the model we have assumed as in previous works (e.g. Richard et al. 2014), a mass-traces-light approach for these galaxy-scale components, where the geometry (center, ellipticity and position angle) follow the light distribution and the other dPIE parameters are scaled with respect to the values of an L* galaxy (σ^*, $r_{\rm core}$, and $r_{\rm cut}$). The two exceptions are the BCG and the brightest galaxy located in the arc, whose σ and $r_{\rm cut}$ parameters are fit independently. Regarding the cluster-scale component, we only assumed $r_{\rm cut} = 1000$ kpc as it is unconstrained. In total, our model is comprised of 12 free parameters.

Regarding the constraints, we have complemented the constraints used in Richard et al. (2010) and reach 13 multiple systems of matched clumps in the giant arc, forming a total of 33 multiple images, all of them are included at their spectroscopic redshift. Unfortunately the Einstein radius is too small and the MUSE data is not deep enough to provide us with additional spectroscopic redshifts for multiple images. Accounting for the image multiplicity and the unknown source location, these clump locations give us 40 constraints, which gives us a well-constrained model with regard to the 12 free parameters. The 33 multiple images of the clumps used to constrain the lens model are shown in Fig. B1 as red circles.

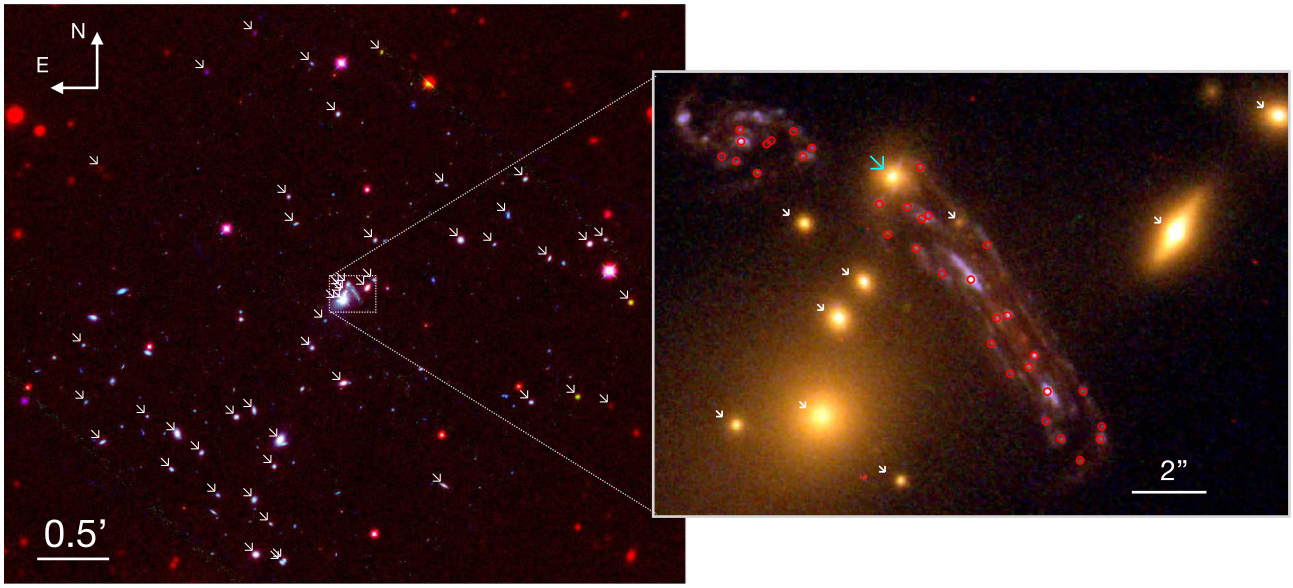

Figure B1. A521 cluster members (white arrows) and multiple images used to constrain the lens model (red circles). The inset show a zoom-in to the central region of the cluster, containing the BCG, the galaxy GAL1 (large cyan arrow) and the images of A521-sys1.

Table B1. Best-fitting parameters of the LENSTOOL mass model.

Potential	$\Delta\alpha$ [arcsec]	$\Delta\delta$ [arcsec]	e	θ [deg]	$r_{\rm core}$ [kpc]	$r_{\rm cut}$ [kpc]	σ [km s^{-1}]
DM1	$-0.7^{+0.2}_{-0.2}$	$-0.5^{+0.2}_{-0.3}$	$0.65^{+0.02}_{-0.03}$	$53.2^{+0.2}_{-0.2}$	23^{+1}_{-1}	[1000]	610^{+4}_{-5}
BCG	[0.0]	[− 0.0]	[0.24]	[47.6]	[0]	81^{+47}_{-18}	215^{+33}_{-12}
GAL1	[2.1]	[6.8]	[0.13]	[58.0]	[0]	5^{+1}_{-1}	27^{+29}_{-50}
L* galaxy					[0.15]	10^{+3}_{1}	180^{+4}_{-13}

The best-fitting parameters of the LENSTOOL mass model are presented in Tab B1. This model gives us an rms of 0.08 arcsec between the observed and the predicted location of all constraints, which is close to the precision of the *HST* locations. The velocity dispersion of the main dark matter halo (cluster-scale) component is ∼600 km s^{-1}, again confirming that the lens is somewhere in between a massive group and a low-mass cluster.

APPENDIX C: MINIMUM RESOLVABLE SIZE

In order to test what is the minimum clump size measurable with our method, we simulate synthetic sources with asymmetric Gaussian profiles and we fit them in the same way as the real clumps. In more details, we produce three sets of synthetic sources with axis ratios uniformly distributed in the ranges [1.0; 1.5], [1.5; 2.0], and [2.0; 4.0], respectively. We add a fourth set of sources with axial ratio fixed at $axr = 1.0$, i.e. with a fixed circular symmetric Gaussian profile. For each set, we simulate 500 sources with sizes uniformly distributed in the range $\log(\sigma_{x,\rm in}/[\rm pixels]) = [-2; 0.6]$, fluxes uniformly distributed in the range $\log(\rm flux_{in}/[e/s]) = [0.0; 0.5]$ and random angle θ. These ranges are chosen to cover the range of properties of the A521-sys1 clump catalogue. The sources are introduced at a random position in the region of the observations covered by the images of the A521-sys1 galaxy and then fitted one at a time in order to avoid the manually-introduced crowding we would have by adding all the 500 sources together.

We define the Gaussian standard deviations derived from the fit as $\sigma_{x,\rm out}$ in contrast to the intrinsic ones, used as input for the simulated clusters, $\sigma_{x,\rm in}$. We consider good fits the ones, where the relative difference $\sigma_{x,\rm rel} \equiv |\sigma_{x,\rm out} - \sigma_{x,\rm in}|/\sigma_{x,\rm out}$ is less than 0.2, i.e. the relative error on the retrieved size is less than 20 per cent. We show the results of the test in Fig. C1. In the left-hand panel, it can be observed how the fraction of good fits steeply increases for $\sigma_{x,\rm out} > 0.4$ pixels. Above this value, the fraction of good fits stabilizes above ∼50 per cent with a clear dependence on the axial ratio, as for more circular sources better fits are returned on average. If, instead of σ_x, we consider the geometrical mean of the minor and major axes of the Gaussian $\sigma_{xy} \equiv \sqrt{\sigma_y \cdot \sigma_y} = \sigma_x \sqrt{axr}$, as done for estimating the effective radius of the real clumps, we see that the fraction of good fits with $\sigma_{xy} > 0.4$ flattens to a value ∼80 per cent, indicating that, for large axr, the derived σ_{xy} is more robust than σ_x and σ_y, considered alone. We observe a small decline of the fraction of good fits for large sizes, possibly driven by their lower average surface brightness. We deal in detail with the completeness in surface brightness in Appendix D. We consider $\sigma_x = 0.4$ pixels as the lowest size recognizable by our routine as below such value the derived sizes seem to be totally uncorrelated to the input values. We use $\sigma_{x,\rm out}$ instead of $\sigma_{x,\rm in}$ as reference as this is the quantity we derive for the real clumps.

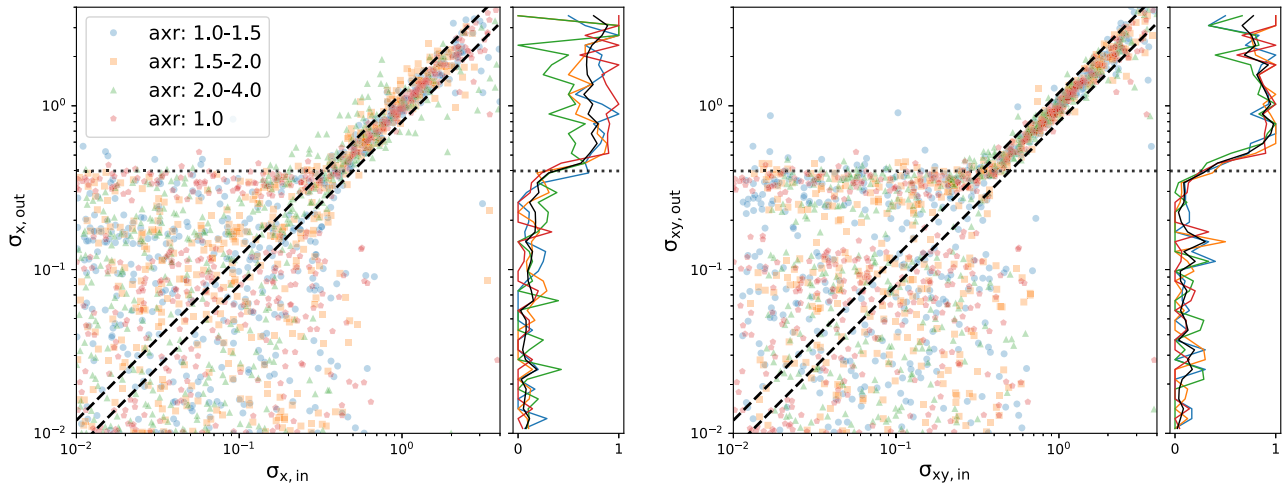

Figure C1. Standard deviation resulting from the fit of synthetic sources in function of their input values. Left-hand panel shows σ for the minor axis (σ_x), right-hand panel shows the geometrical mean $\sigma_{xy} \equiv \sqrt{\sigma_x \cdot \sigma_y}$. Different colours and symbols refer to sources with different axis ratios, as reported in the legend. The dashed lines enclose the good fits, i.e. where the relative error on the retrieved size is less than 20 per cent. The horizontal dotted line mark the $\sigma_{x,\mathrm{min}} = 0.4$ pixels value chosen as the minimum resolvable size. For each panel, the subpanel on the side shows the fraction of sources with good fit in function of the output standard deviation.

APPENDIX D: COMPLETENESS TEST

We test the luminosity completeness of our observation in a similar way as described in Appendix C, i.e. by introducing synthetic sources in the field of view of the galaxy and fitting them in the same way as for the real clumps. We use the map of the galaxy after having subtracted the flux of the real clumps. Despite the fact that most of the observed clumps have profiles consistent with the instrumental PSF, we simulate sources with different sizes in order to derive a surface brightness limit. In more details, we simulate three sets of clumps with $\sigma_x = 0.4$, 1.0, and 2.0 pixels (0.024, 0.06, and 0.12 arcsec, respectively), sources with larger sizes are not measured in this galaxy and therefore are not necessary to be simulated. For all sets, we simulate circularly symmetrical sources, i.e. we set $axr \equiv 1$. For each set we simulate 500 sources with fluxes randomly drawn from a uniform distribution in the range $(\mathrm{flux}_\epsilon/[\mathrm{e/s}]) = [-2.0; 1.0]$ for sources with $\sigma_x = 0.4$ and 1.0 pixel, and in the range $\log(\mathrm{flux_{in}}/[\mathrm{e/s}]) = [-1.0; 2.0]$ for sources with $\sigma_x = 2.0$ pixels.

Some of the synthetic clumps have recovered fluxes $\mathrm{flux_{out}}$ consistent with zero ($<10^{-4}$ e/s, i.e. more than two orders of magnitude lower than the input values), meaning that the fitting process do not recognize the source and consider the cut-out as only filled by background emission. Those are 27 sources with $\sigma_{x,\mathrm{in}} = 0.4$ pixel and $\mathrm{flux_{in}} < 0.07$ e/s (28.3 mag), 31 with $\sigma_{x,\mathrm{in}} = 1.0$ pixel and $\mathrm{flux_{in}} < 0.12$ e/s (27.7 mag), and 11 with $\sigma_{\mathrm{in}} = 2.0$ pixels and $\mathrm{flux_{in}} < 0.39$ e/s (26.4 mag). We call these $\mathrm{flux_{in}}$ values detectability limits, $\mathrm{lim_{det}}$. We observe that some of the sources with fluxes higher than the detectability limits are still not well-fitted and we therefore investigate the precision in recovering the input properties.

We calculate for each of the synthetic sources the relative error on the recovered flux, i.e. $\mathrm{flux_{rel}} = |\mathrm{flux_{in}} - \mathrm{flux_{out}}|/\mathrm{flux_{in}}$. The values of $\mathrm{flux_{rel}}$ are clustered around zero for bright sources, but they start deviating to larger values (suggesting larger uncertainties in fitting the source) when considering dimmer sources. The cases where the relative error on the recovered flux is above 50 per cent, i.e. $\mathrm{flux_{rel}} \geq 0.5$ can be considered unreliable fits. We plot the fraction of acceptable fits satisfying $\mathrm{flux_{rel}} < 0.5$ in function of $\mathrm{flux_{in}}$ in the left-hand panel of Fig. D1. We name the flux values at which the fraction goes above 80 per cent completeness limits $\mathrm{lim_{com}}$, these are more conservative values compared to the detectability limits described above. The completeness limits for the three sets of sources are $\mathrm{lim_{com,0.4}} = 0.15$ e/s (27.5 mag), $\mathrm{lim_{com,1.0}} = 0.30$ e/s (26.7 mag), and $\mathrm{lim_{com,2.0}} = 1.20$ e/s (25.2 mag). We repeat this process by calculating the relative error on the recovered size, i.e. $\sigma_{\mathrm{rel}} = |\sigma_{\mathrm{in}} - \sigma_{\mathrm{out}}|/\sigma_{\mathrm{in}}$, and plotting the fraction of acceptable fits with $\sigma_{\mathrm{rel}} < 0.5$ in the right-hand panel of Fig. D1. The $\mathrm{flux_{in}}$ values corresponding to fractions above 80 per cent are the same or smaller than $\mathrm{lim_{com}}$ discussed above therefore we kept the latter as more conservative values. In Section 4.1 of the main text, we compare $\mathrm{lim_{com}}$ values found with this analysis to the magnitudes of the observed clumps. As final remark, we tested an average completeness over the entire area covered by the three images of A521-sys1, keeping separated the three regions defined in Section 2.1 would not affect very much the values recovered.

APPENDIX E: EXTINCTION MAP FROM MUSE

We leverage the VLT-MUSE observations of A521 to estimate the nebular extinction of the galaxy. The spectrum at the redshift of A521-sys1 covers the wavelengths of two Balmer lines, namely H γ and H δ. At fixed gas density and temperature these lines have a fixed ratio i.e. $R_{\gamma\delta,\mathrm{intr}} \equiv L_{\mathrm{H}\gamma}/L_{\mathrm{H}\delta} = 1.81$ for electron density $n_e = 10^2\,\mathrm{cm^{-3}}$ and electron temperature $T_e = 10\,000$ K. The ratio change only by ± 0.01, if T_e varies in the range 5000–20 000 K (values from Dopita & Sutherland 2003, based on Storey & Hummer 1995). A non-zero extinction changes the value of the ratio by a factor proportional to the magnitude of the extinction itself. We can use the observed line ratio $R_{\gamma\delta,\mathrm{obs}}$ to derive the colour excess $E(B-V)$ from:

$$R_{\gamma\delta,\mathrm{obs}} = R_{\gamma\delta,\mathrm{intr}} \cdot 10^{0.4 \cdot E(B-V)[k(\mathrm{H}\gamma) - k(\mathrm{H}\delta)]} \quad \text{(E1)}$$

where $k(\mathrm{H}\gamma)$ and $k(\mathrm{H}\delta)$ are set by the extinction curve considered, in this case the Milky Way one (Cardelli et al. 1989). We divide the

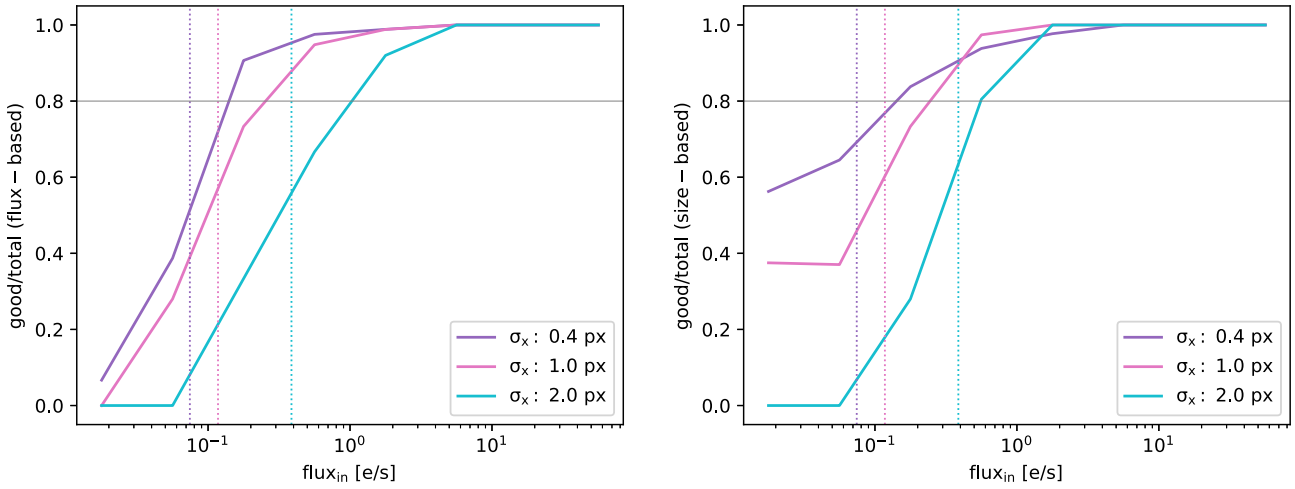

Figure D1. Fraction of good fits over the total number of simulated sources in function of the input flux of the sources, $\mathrm{flux_{in}}$. Good fits are defined as the ones whose relative flux (left-hand panel) or size relative error (right-hand panel) is below 50 per cent. Each 'completeness' curve refer to a different input size (0.4, 1.0, and 2.0 pixels for purple, pink, and cyan curve, respectively). The horizontal line indicate 80 per cent completeness used to derive the completeness limits ($\mathrm{lim_{com}}$, defined as the flux values where the curves reaches the 80 per cent completeness). The dotted vertical lines refer to the detection limits $\mathrm{lim_{det}}$ described in the text.

galaxy in six concentric annular regions with radii of 2 kpc, using the source-plane image to define the annuli and transposing them to the CI, LN, and LS images using the lensing model, as described in Nagy et al. (2021). This division assumes that the largest extinction differences would appear studying the galaxy radially.

In each of the six bins, we use the pPXF tool (Cappellari 2017) to fit and subtract the spectral continuum (including self-absorption of the lines) and the PYPLATEFIT tool to perform the line fit of the H γ and H δ lines.[4] Before deriving $R_{\gamma\delta,\mathrm{obs}}$ we de-redden the line flux for the Milky Way extinction ($\mathrm{A_{V,MW}} = 0.21$ mag), using the Cardelli et al. (1989) extinction function. We consider the same extinction function to derive $E(B-V)$ in equation (E1).

The derived $E(B-V)$ values are shown in Fig. E1 along with the uncertainties coming from the line and continuum fitting. Due to the large uncertainties, all values are consistent within 1σ with zero extinction. However, we notice that extinction in the three internal bins is consistently higher than in the external bins (where the face values goes to unphysical negative values). The outermost bin has lower S/N compared to the other ones, translating into very large uncertainties that makes it unreliable. If differential extinction is considered, as in Calzetti et al. (2000), the nebular extinction we derived should be rescaled, $E(B-V)_{\mathrm{star}} = 0.44 \cdot E(B-V)_{\mathrm{gas}}$, in this case, the stellar extinction within the galaxy would be even lower.

Despite not being able to put hard constraint on the extinction values, this analysis suggests the presence of only low average extinction in A521-sys1, ranging up to $E(B-V) \approx 0.5$ mag in the internal regions and close to $E(B-V) \approx 0.0$ mag in the outskirts. These overall values are consistent with the extinction values of the individual clumps, mainly distributed in the range $E(B-V)$ range 0.0–0.5 mag (Section 5).

[4]PYPLATEFIT is a tool developed for the MUSE deep fields and is a simplified python version of the PLATEFIT IDL routines developed by Tremonti et al. (2004) and Brinchmann et al. (2004) for the SDSS project.

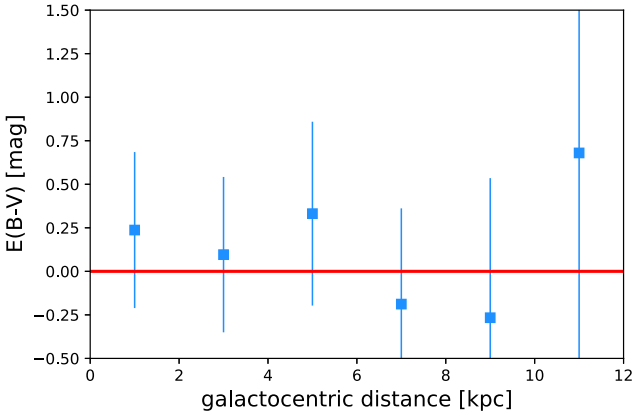

Figure E1. Colour excess values $E(B-V)$, derived from the MUSE data in six concentric annular subregions of A521-sys1 of 2 kpc radius. The values are derived assuming an electron temperature $T_e = 10^4$ K. The unphysical uncertainty on last bin is due to the low signal in the outskirts of the galaxy. We consider the (non-physical) negative values as consistent with no extinction.

APPENDIX F: COMPARISON BETWEEN FIDUCIAL AND ALTERNATIVE EXTRACTION AND PHOTOMETRY

To test the reliability of our results, we implement an alternative method for extracting and analysing the clumps. We measure the properties of the galactic diffuse background (median value and standard deviation, σ) in a region within the galaxy devoid of clumps. We use contours at 3σ level (using a smoothing of three pixels) above the median value of the background to extract clumps and define their extent. The sizes of clumps are calculated using ellipses that better trace the 3σ contours. We used 6σ contours to separate multiple peaks within the same 3σ contours, considering them as separate clumps. When two 6σ peaks are in the same 3σ contour, two ellipses are considered trying to cover the entire region within the contour without intersecting them. We consider the geometric mean of the major and minor axis of each ellipses, $R_3 = \sqrt{ab}$, where the subset

3 is used to indicate that this radius refer to the extent of the 3σ contours. In order to convert R_3 into an effective radius we assume that clumps have Gaussian profiles and we first derive an *observed* effective radius:

$$R_{\rm eff,obs} = R_3 \sqrt{\frac{\ln(2)}{\ln(r_{\rm peak}/3)}}, \tag{F1}$$

where $r_{\rm peak}$ is the ratio of the peak of each region over the RMS value. Then we find the intrinsic effective radius by subtracting, in quadrature, the HWHM of the instrumental PSF, which, for F390W, is 0.8 pixel,

$$R_{\rm eff} = \sqrt{R^2_{\rm eff,obs} - 0.8^2}. \tag{F2}$$

Where $R_{\rm eff,obs}$ is smaller than the *HWHM* of the PSF we set manually the intrinsic $R_{\rm eff}$ to the minimum value detectable, $R_{\rm eff,min} = \sigma_{x,\rm min}\sqrt{2\ln 2} \approx 1.8\sigma_{x,\rm min} = 0.47$ pixel, described in Section 3.2.2.

Photometry is performed using aperture photometry in the ellipses defined above, and subtracting the background estimated as the median value of the sky evaluated in a annular region around the aperture. Aperture correction is needed to correct the flux for losses due to finite apertures. We simulate sources with the sizes found using equation (F2), we perform aperture photometry using the same apertures used on the real data and then we calculate what is the fraction of flux we are missing. The missing flux is then converted into an aperture correction, we therefore have a specific aperture correction for each source. The values hence found may constitute in some cases overestimates, some of the clumps present a bright peak and then some more diffuse light filling the 3σ contour and the assumption of a 2D-Gaussian profile may not be accurate in these cases. The conversion of sizes from pixels to parsecs and of flux into observed and absolute magnitudes is done in the same way as for the reference sample, as well as the de-lensing[5] and the SED fitting (see Sections 3.3 and 3.4).

[5]The only exception that we use different apertures, i.e. the ones also used for photometry to estimate the median amplification factors and their uncertainties.

This paper has been typeset from a TEX/LATEX file prepared by the author.